



Utrecht University
Graduate School of Natural Sciences

**Measurement of Z boson Production
in the Muon Decay Channel in Lead-Lead Collisions
at $\sqrt{s_{NN}}=2.76\text{TeV}$ with the ATLAS detector**

J. Onderwaater

August 12, 2012

Report number: UU(SAP) 12-X

Supervisors: Prof. dr. T. Peitzmann and dr. A. Milov

Institute of Subatomic Physics

Buys Ballot laboratory

PO BOX 80 000, 3508 TA Utrecht, The Netherlands

DISCLAIMER

The research for this thesis was conducted as a visiting student at the Feinberg Graduate School of the Weizmann Institute of Science in Rehovot, Israel under the supervision of dr. Alexander Milov, and as a member of the ATLAS collaboration of the European Laboratory for Particle Physics (CERN).

ABSTRACT

The ATLAS detector at the LHC recorded data with an integrated luminosity of $142\mu\text{b}^{-1}$ from lead-lead collisions at $\sqrt{s_{NN}} = 2.76$ TeV. A sample of 1223 Z bosons was reconstructed through the muon decay channel with high purity, enabling the most accurate measurement in heavy ion collisions conducted with Z bosons so far. The Z boson properties are studied as a function of transverse momentum and rapidity. The production rate of the Z boson is measured differentially with event centrality. Furthermore the azimuthal distribution of the Z boson emission with respect to the event plane is used to uncover potential modifications due to the collision geometry. Within statistical and systematic uncertainties, the per-event yield is proportional to the number of binary collisions estimated by the Glauber model, and the flow of the Z boson is found to be consistent with zero.

Contents

1	Introduction	5
2	Theory	7
2.1	Z boson production	7
2.2	Total and partial widths of the Z boson	9
2.3	Particle decays	10
2.4	Heavy Ion collision geometry	10
2.5	The Glauber Model	12
2.6	Centrality estimation	13
2.7	Quark-gluon plasma	15
2.8	QGP signatures	16
3	The ATLAS experiment	19
3.1	Large Hadron Collider	19
3.2	ATLAS detector	21
3.3	Inner detector	23
3.4	Muon spectrometer	23
3.5	Forward detectors	24
3.6	Triggers	24
3.7	Muon reconstruction algorithms and track fitting	24
4	Analysis	29
4.1	ATLAS data and stability	29
4.2	Single muon reconstruction	32
4.3	$Z \rightarrow \mu^+\mu^-$ reconstruction	38
4.4	Correction strategy	49

4.5	Systematic uncertainties	51
5	Results	57
5.1	Summary and Conclusion	62

Chapter 1

Introduction

At the beginning of this millenium evidence emerged of a new and exciting state of matter. Heavy ion programs carried out at the Relativistic Heavy Ion Collider (RHIC) at BNL, and the Large Hadron Collider (LHC) at CERN, have established that a hot and dense matter is produced in relativistic heavy ion collisions. This matter embodies a state where quarks and gluons are deconfined. This medium imposes significant energy loss on energetic color charge carriers that pass through [1, 2]. An understanding of the modification requires accurate knowledge of the production rates of particles before they loose energy. To this end several studies have focused on particles unmodified by the medium. The PHENIX experiment at RHIC measured highly energetic photons [3], and the ATLAS and CMS experiments provided the first measurements of Z , W and photons at the LHC energy [4, 5, 6, 7]. The results shown so far, based on measurements from the 2010 LHC heavy ion running, are limited in statistics but were able to show that the production rate in heavy ion collisions of particles with high momentum transfer are proportional to the mean number of binary collisions, $\langle N_{\text{coll}} \rangle$. This corresponds to a representation of the heavy ion collision as a superposition of individual nucleon-nucleon collisions.

An interesting evolution of the measurement is to correlate particles modified by the medium to unmodified particles, the first providing a handle to accurately study medium effects imposed on the latter. An example of this is Z -jet events. The Z boson is a heavy color neutral boson supposedly unaffected by the medium, while the jet originating from quark production will undergo modifications [8]. If reliable results should emerge from this measurement however it is essential to prove that the Z is in fact, as predicted, unmodified by the medium. This is the subject of this thesis, where a precise measurement of Z boson production in lead-lead collisions at $\sqrt{s_{NN}} = 2.76$ TeV using the muon decay channel is presented.

The thesis is organized as following. In the next chapter some of the theoretical ground-work is laid down, providing background for the mechanisms studied but also explanations of the tools used in the analysis. The third chapter contains details of what makes everything possible: the machinery. From the immense particle accelerator to the massive ATLAS detector and down to the reconstruction algorithms, an overview is given covering essential building blocks before any physics analysis can be started. In chapter four, the many details of the analysis are carefully described, before arriving at chapter

five, the results.

The ATLAS detector also measures Z bosons in the electron channel. For consistency and an increase of the number of Z bosons measured, the muon channel was studied in parallel with the electron channel. The electron analysis is not included in this thesis, but the framework for both analyses the data, analysis methods and presentation of the results are to far extent the same, and conducted in cooperation. The results, with both lepton channels combined, demonstrate that the production of Z bosons in heavy ion collisions is proportional to $\langle N_{\text{coll}} \rangle$, as parametrized by the Monte Carlo Glauber Model. Inspection of the Z emission angle with respect to the second order event plane shows that the elliptic flow coefficient v_2 of the Z boson is consistent with the view of a particle unaffected by the asymmetric shape of the initial collision geometry.

Chapter 2

Theory

This chapter contains descriptions of theoretical topics related to several parts of the analysis performed with ATLAS data. These concern the production and decay of the Z boson, the properties of the quark gluon plasma (QGP) and the type of measurements that can help to understand the latter.

2.1 Z boson production

The Z boson, the neutral mediator of the weak force, is mostly created through the the Drell-Yan process ($q\bar{q} \rightarrow Z \rightarrow \mu\mu$) shown in Figure 2.1. The Drell-Yan process can occur with or without initial-state gluon radiation. Z bosons can also be produced in association with jets, as is shown in Figure 2.2.

In the Drell-Yan mechanism one quark from one of the nucleons from one the impending nuclei annihilates with an antiquark from the other nucleus into a vector boson (either a photon, W or Z) with a large invariant mass. When pictured in a proton-proton collision, the momentum transfer can be written as

$$Q^2 = (x_1 p_1 + x_2 p_2)^2 = M_{Z,W,\gamma}^2, \quad (2.1)$$

where x_i is the momentum carried by a parton as a fraction of proton momentum p_i . To leading order (LO) the double differential Drell-Yan scattering cross section for the

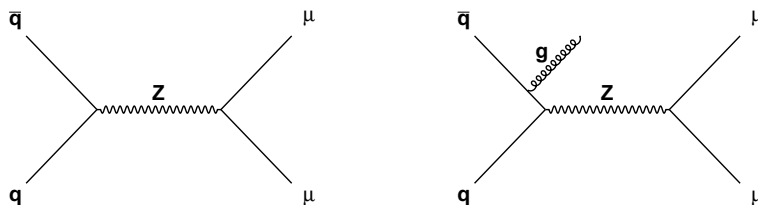


Figure 2.1: *Left*: Z boson production through $q\bar{q}$ annihilation, also known as the Drell-Yan channel. *Right*: NLO process consisting of Drell-Yan Z production with initial-state gluon radiation.

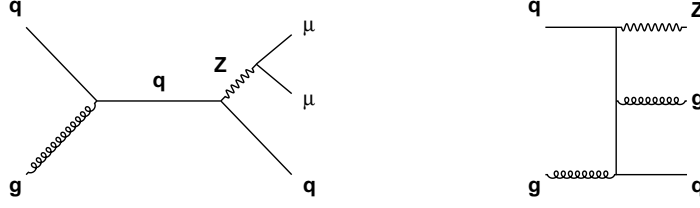


Figure 2.2: *Left*: Z boson production through gluon Compton scattering resulting in a $Z + 1$ jet event. *Right*: NNLO process consisting of a $Z + 2$ jet event.

neutral current (NC) reaction $p+p \rightarrow (Z/\gamma)X \rightarrow \mu\mu X$ can be written as [9]

$$\frac{d^2\sigma}{dMdy} = \frac{4\pi\alpha^2(M)}{9} 2M P(M) \Phi(x_1, x_2, M^2). \quad (2.2)$$

Here M is the invariant mass of the Z decay products and y is the boson rapidity. $P(M)$ is a propagator term and Φ a parton distribution function. In the NC Drell-Yan process, the boson can either be a photon or a Z . In case of photon exchange $P(M)$ and Φ are given by

$$P_\gamma(M) = \frac{1}{M^4}, \quad \Phi_\gamma = \sum_q e_q^2 F_{q\bar{q}}, \quad (2.3)$$

$$F_{q\bar{q}} = x_1 x_2 [q(x_1, M^2) \bar{q}(x_2, M^2) + \bar{q}(x_1, M^2) q(x_2, M^2)]. \quad (2.4)$$

Here e_q is the electric charge of quarks. The corresponding γZ interference term is described by

$$P_{\gamma Z} = \frac{\kappa_Z v_\mu (M^2 - M_Z^2)}{M^2 [(M^2 - M_Z^2)^2 + (\Gamma_Z M_Z)^2]}, \quad \Phi_{\gamma Z} = \sum_q 2e_q v_q F_{q\bar{q}}, \quad (2.5)$$

$$v_f = I_3^f - e_f \sin^2 \Theta, \quad a_f = I_3^f [f = \mu, q], \quad \kappa_z = \frac{1}{4 \sin^2 \Theta \cos^2 \Theta}, \quad \cos \Theta = \frac{M_W}{M_Z}. \quad (2.6)$$

The interference contribution is proportional to the vector coupling of the muon v_μ . For the muon, $I_3^\mu = -1/2$ (see Table 2.2) and as $\sin^2 \Theta \approx 1/4$, v_μ is small which means contribution of the γZ interference term cross section is also small. The pure Z exchange can be written as

$$P_Z = \frac{\kappa_Z^2 (v_\mu^2 + a_\mu^2)}{(M^2 - M_Z^2)^2 + (\Gamma_Z M_Z)^2}, \quad \Phi_Z = \sum_q (v_q^2 + a_q^2) F_{q\bar{q}}. \quad (2.7)$$

As shown in the left of Figure 2.3, the pure Z term dominates around 90 GeV while the photon term dominates at low mass. At high mass the photon and Z contribution to the cross section is similar. On the right side can be seen that the cross section for Z boson production is correlated with the center of mass energy, as the coupling constants run with energy. At the heavy ion LHC energy of $\sqrt{s_{NN}} = 2.76$ GeV with the Z cross section with decay to the lepton channel is approximately 0.3 nb.

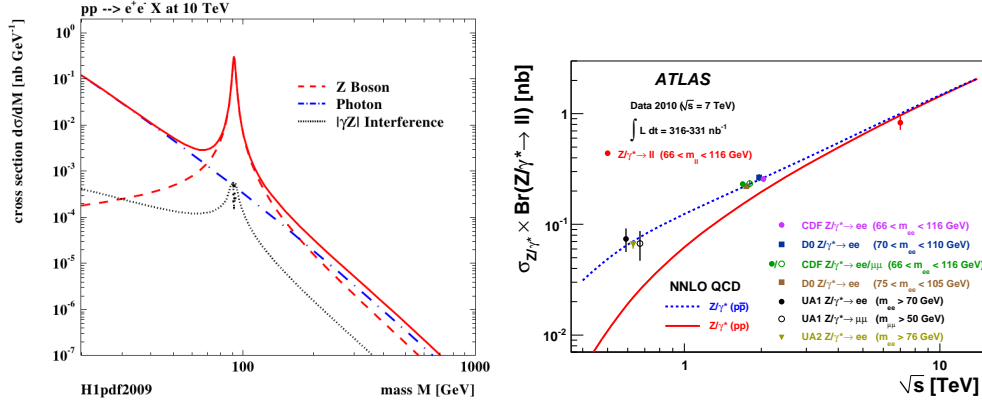


Figure 2.3: *Left:* $Z \rightarrow ee$ cross section as a function of invariant mass integrated over the boson rapidity y^Z . The Z resonance determines the cross section around 90 GeV, at low mass photons have the main contribution and at large mass both boson contributions are similar [9]. *Right:* Production cross section for Z bosons in the energy domain in the LHC decaying through the lepton channel. The theoretical predictions based on NNLO QCD calculations are shown for proton-proton and proton-antiproton colliders as a function of \sqrt{s} [10].

2.2 Total and partial widths of the Z boson

The Z boson is unstable and decays after a very short time (in the order of 10^{-24} s) into quark and lepton pairs. The most dominant decay modes are listed in Table 2.2. Approximately 70% decays into quark pairs and another 20% to neutrino pairs. The remaining 10% consists of decays to charged lepton flavours. The three channels are equally likely since coupling of the leptons to gauge bosons is flavour-independent. The partial width of any of the modes is

$$\Gamma(\text{partial}) = \frac{G_F M_Z^3 \rho}{6\pi \sqrt{2}} (c_A^2 + c_V^2) F. \quad (2.8)$$

Here G_F is the Fermi Constant. For the case that the Higgs boson is not a scalar but has a more complex isospin structure a factor is included that modifies the relative magnitude of the neutral current compared to the charged current, $\rho = M_W^2/M_Z^2 \cos^2 \theta_W$ (to date experimentally 1). c_A and c_V are the axial vector coupling factors, see Table 2.2. The values of F are:

$$\begin{aligned} Z \rightarrow \nu\nu, & \quad F = 1, \\ Z \rightarrow \ell\ell, & \quad F = (1 + 3\alpha/4\pi), \\ Z \rightarrow Q\bar{Q}, & \quad F = 3(1 + \alpha_s/\pi). \end{aligned}$$

Here α and α_s are the running coupling constants. For leptons, F represents a QED corrections for final state radiation (FSR) of photons. For the decay to quark pairs F contains a colour factor ($N_c = 3$) and another QCD factor for gluon radiation by the quarks. A calculation of the total width based on the assumption of $N_\nu = 3$ neutrino flavours results in $\Gamma_{\text{total}} = 2.49$. This assumption was confirmed later in experiment and has the current measured value $\Gamma_{\text{total}} = 2.4952 \pm 0.0023$ [11].

Mode	Fraction (Γ_i/Γ)	Particle	vector	axial
ee	(3.363 ± 0.004) %	e	-0.038	-0.5
$\mu\mu$	(3.366 ± 0.007) %	μ	-0.038	-0.5
$\tau\tau$	(3.370 ± 0.008) %	τ	-0.038	-0.5
$\ell\ell$	(3.3658 ± 0.0023) %	ν_e	0.5	0.5
invisible	(20.00 ± 0.06) %	ν_μ	0.5	0.5
hadrons	(69.91 ± 0.06) %	ν_τ	0.5	0.5
(uu+cc)/2	(11.6 ± 0.6) %	u	0.192	0.5
(dd + ss +bb)/3	(15.6 ± 0.4) %	d	-0.346	-0.5
cc	(12.03 ± 0.21) %	c	0.192	0.5
bb	(15.12 ± 0.05) %	s	-0.346	-0.5
g g g	< 1.1 %	t	0.192	0.5
		b	-0.346	-0.5

Table 2.2: *Left:* Decay modes of the Z boson [11]. *Right:* List of axial and vector couplings for fermions assuming $\sin \theta_W = 0.231$ [12].

2.3 Particle decays

The properties of a very shortlived particle like the Z boson can only be recovered through the properties of the decay products. A 4-vector q of each decay product is formed with their energy E and 3-momentum \mathbf{p} : $q = (E, \mathbf{p})$. The inner product of the parent 4-vector corresponds to the invariant mass $q^2 \equiv E^2 - |\mathbf{p}|^2 = m^2$ of the system. It can be calculated with 4-momentum conservation from the 4-vectors of all j daughter particles as follows

$$\begin{aligned}
 q^2 &= (\sum_{i=1}^j q_i)^2 \\
 &= \left(\sum_{i=1}^j E_i \right)^2 - \left(\sum_{i=1}^j \mathbf{p}_i \right)^2 \\
 &= m^2.
 \end{aligned} \tag{2.9}$$

The full 4-vector of the mother particle is then recovered with $q = \left(\frac{m^2 + \mathbf{p}^2}{2}, \mathbf{p} \right)$, with $\mathbf{p} = \sum_{i=1}^j \mathbf{p}_i$. It will be relevant to recover the kinematic parameters of the mother particle in the detector coordinate system:

$$\begin{aligned}
 y &= \frac{1}{2} \ln \frac{E + p_z}{E - p_z}, \\
 \phi &= \arctan(p_y, p_x).
 \end{aligned} \tag{2.10}$$

2.4 Heavy Ion collision geometry

In the LHC two soon-to-collide lead ions move towards at each other close to the speed of light. In the lab frame, the usual spherical shape of the nuclei becomes Lorentz contracted along the beam direction. The flattened volumes approach each other with a Lorentz invariant displacement from center-to-center called the impact parameter b .

Following the *optical limit* approximation, it is assumed that the nucleons carry sufficient momentum that the nucleons will essentially move undeflected through each other, as depicted in Figure 2.4. For a matter of generality the projectiles shown here have different radii (as for instance in Cu+Au collisions). During the collision an overlap area of the nuclei is created. Let us focus on a small area at a displacement s with respect to the center of the target nucleus and a distance $s - \mathbf{b}$ from the center of the projectile (which nucleus is the projectile and the target is just a matter of preference for colliding beam experiments). The probability per unit transverse area of a given nuclon existing in that location is $\hat{T}_A(s) = \int \hat{\rho}_A(s, z_A) dz_A$, with $\hat{\rho}(s, z_A)$ the probability per unit volume, normalized to unity, for finding the nucleon at location (s, z_A) . A similar expression follows for the projectile nucleus. The probability per unit area for nuclons being located at the displacement for both the projectile and the target is the product of the two $\hat{T}_A(s)\hat{T}_B(s - \mathbf{b})d^2s$. The integral over all values of s defines the *thickness function* $\hat{T}(\mathbf{b})$, with

$$\hat{T}_{AB}(\mathbf{b}) = \int \hat{T}_A(s)\hat{T}_B(s - \mathbf{b})d^2s. \quad (2.11)$$

The thickness function has the unit of inverse area. It can be interpreted as an effective overlap area for which a given nucleus in A can interact with a given nuclon in B. The probability of an interaction occurring is given by $\hat{T}(\mathbf{b})\sigma_{\text{inel}}^{\text{NN}}$, where $\sigma_{\text{inel}}^{\text{NN}}$ is the inelastic nucleon-nucleon cross section. One can express the probability for n inelastic interactions between nuclon A and B (with A and B nuclons respectively) as a binomial distribution:

$$P(n, \mathbf{b}) = \binom{AB}{n} [\hat{T}_{AB}(\mathbf{b})\sigma_{\text{inel}}^{\text{NN}}]^n [1 - \hat{T}_{AB}(\mathbf{b})\sigma_{\text{inel}}^{\text{NN}}]^{AB-n}, \quad (2.12)$$

where the first term gives the number of possible combinations that give n interactions, the second term represents the probability for having n interactions and the last term the probability of having a complementary number $(AB - n)$ of misses. The summation over all possible number of n interactions will naturally give the total probability of at least one interaction occurring,

$$\frac{d^2\sigma_{\text{inel}}^{\text{AB}}}{db^2} \equiv p_{\text{incl}}^{\text{AB}}(b) = \sum_{n=1}^{AB} P(n, \mathbf{b}) = 1 - [1 - \hat{T}_{AB}(\mathbf{b})\sigma_{\text{inel}}^{\text{NN}}]^{AB}. \quad (2.13)$$

If the orientation of the colliding nuclei is random, i.e. the nuclei are not polarized, the vector \mathbf{b} can be replaced by a scalar and the total cross section can be written as

$$\sigma_{\text{inel}}^{\text{AB}} = \int_0^\infty 2\pi b db \left\{ 1 - [1 - \hat{T}_{AB}(b)\sigma_{\text{inel}}^{\text{NN}}]^{AB} \right\}. \quad (2.14)$$

The expectancy value for the number of collisions as a function of b is

$$N_{\text{coll}}(b) = \sum_{n=1}^{AB} nP(n, b) = AB \hat{T}_{AB}(b)\sigma_{\text{inel}}^{\text{NN}}. \quad (2.15)$$

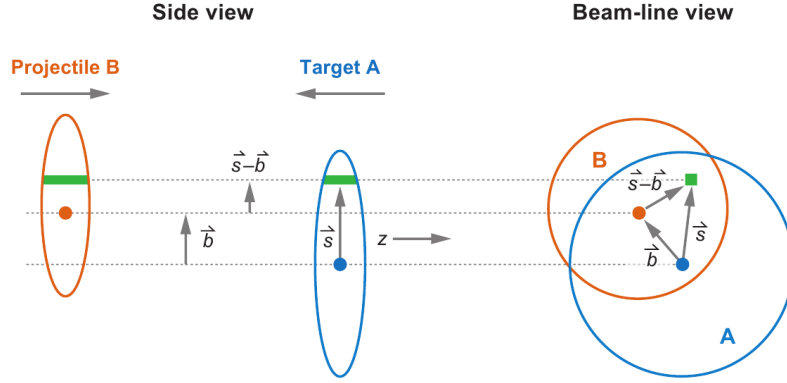


Figure 2.4: The side and beam-line view of two colliding nuclei. The impact parameter determines the overlap shape, which combined with the nuclear density function is used to calculate the probability density of an interaction at a given point.

Finally, the number of nucleons involved in the collisions (N_{part}) the nucleons involved in the collisions are only counted once. This number is given by [13, 14]

$$N_{\text{part}}(\mathbf{b}) = A \int \hat{T}_A(\mathbf{s}) \left\{ 1 - \left[1 - \hat{T}_B(\mathbf{s} - \mathbf{b}) \sigma_{\text{inel}}^{\text{NN}} \right]^B \right\} ds^2 + B \int \hat{T}_B(\mathbf{s} - \mathbf{b}) \left\{ 1 - \left[1 - \hat{T}_A(\mathbf{s}) \sigma_{\text{inel}}^{\text{NN}} \right]^A \right\} ds^2. \quad (2.16)$$

These parameters will be useful to study correlations in event centrality with observations such as particle spectra and flow. But it is necessary to determine the input parameter b , or the event centrality.

2.5 The Glauber Model

High energy collisions of macroscopic objects, like lead nuclei, can be characterized by the emission of a large number of particles. The Glauber model was contrived to describe the underlying structure of this chaotic spectacle. It pictures the nuclei trajectory as a straight line along the collision direction and describes nucleus-nucleus interaction in terms of interaction between the constituent nucleons and nuclear density distribution. As nuclei consist of nucleons, it is a natural concept to think of the colliding systems as a combination of proton-proton, proton-neutron and neutron-neutron collisions. What the model would have to take into account is which nuclei participate, and how often, in the collision. Although this looks like a very complicated problem, there exist a variety of methods to make these estimations that have been developed and improved in the course of various heavy ion experiments.

The Glauber model itself has various input parameters, which are given by experimental data. The most important are the nuclear density distribution and the energy dependence of the inelastic nucleon-nucleon cross section.

The nucleon density can be parametrized by a Fermi distribution (also known as the Wood-Saxon distribution) with three parameters:

$$\rho(r) = \rho_0 \frac{1 + w(r/R)^2}{1 + \exp(\frac{r-R}{a})}, \quad (2.17)$$

where ρ_0 is the nucleon density in the centre in the nucleus, r the distance to that centre, R is the nuclear radius, a to the skin depth, and w characterizes deviations from a spherical shape. For $s^{208}\text{Pb}$, $R = 6.62\text{fm}$, $a = 0.546\text{fm}$ and $w = 0\text{fm}$ [15]. These values are determined in low-energy electron scattering experiments. The Monte Carlo Glauber model, which can be used to determine the number of binary collisions (N_{coll}) and the number of participants (N_{part}), positions nucleons at the correct relative positions. The nucleons move towards each other along straight paths and interact if their transverse distance d is less than the "hard disk" radius, provided by the inelastic nucleon-nucleon cross section $d_0 = \sqrt{s_{NN}/\pi}$. A nucleon is a participant if it interacts at least once. The number of times every participant interacts determines N_{coll} (number of binary collisions).

The cross section of nucleon collisions involves interactions with low momentum transfer, therefore it is impossible to calculate it using perturbative quantum chromodynamics. The cross section used to determine N_{coll} and N_{part} is derived from extrapolations of the elastic and total cross sections, and is taken to be $64 \pm 5\text{mb}$.

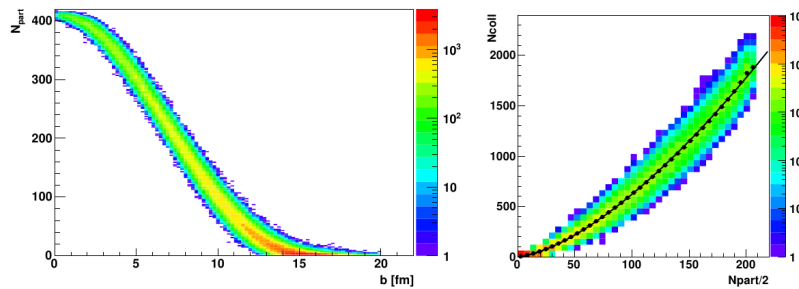


Figure 2.5: The Glauber Monte Carlo results on the number of participants as a function of impact parameter, and the number of binary collisions as a function of participant pairs, and the number of binary collisions as a function of participant pairs. The right figure is plotted with a power law fit showing that $N_{\text{coll}} \propto N_{\text{part}}^{3/2}$

The Glauber Monte Carlo used to produce the results in Figure 2.5 does not assume nuclei to be smooth densities (as in the "optical limit approximation"), but rather takes into account the local density fluctuations event-by-event. The average number of participants and collisions vary monotonically with the impact parameter.

2.6 Centrality estimation

As has become clear from the description of the Glauber model, the impact parameter is an important parameter. Not only for estimation of N_{coll} and N_{part} , but as will be discussed in the section on flow also for the shape of the overlapping area. To define

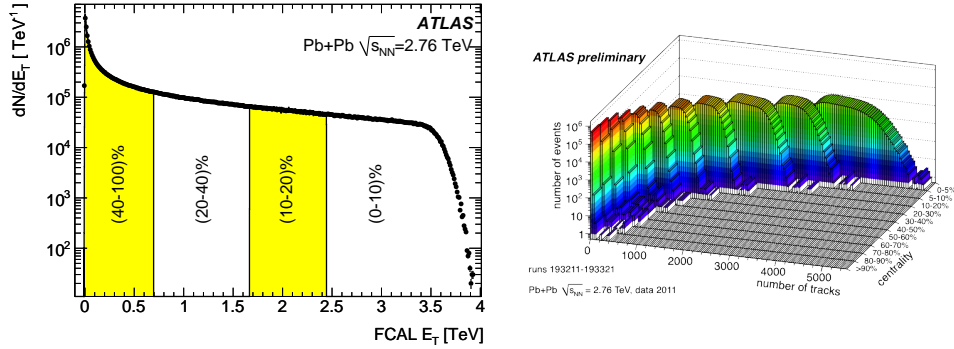


Figure 2.6: left *Left*: Energy deposition in the forward calorimeters (FCal) of the ATLAS detector. The activity in the detectors is directly translated in event centrality classes [16]. *Right*: Track multiplicity in different centrality classes, also constructed with ATLAS data.

centrality classes for the lead-lead collisions experimental quantities (e.g. energy deposition $\sum E_T$ in the calorimeters) are related to a geometric quantity (e.g. N_{coll}). For example the 10% of events with the highest energy deposition should correspond to 10% of events with the highest values of N_{part} . Figure 2.6 shows the total transverse energy ($\sum E_T$) deposited in the forward calorimeters (FCal) of the ATLAS detector, which cover $3.1 < \eta < 4.9$. The FCal is used as opposed to energy deposition in mid-rapidity to avoid biasing the centrality measurement with jets. The energy deposition is directly projected to event centrality classes. The figure on the right hand side shows the track multiplicity in centrality classes determined with the FCal distribution. It demonstrates that the quantities associated with event centrality have overlap in bordering classes. The sharper the falloff of these shapes the more precise the determination of the event centrality. Table 2.1 lists N_{coll} and N_{part} for different centrality bins.

Bin	N_{coll}	N_{part}
0-5%	1683	382.1
5-10%	1318	330.3
10-20%	923	260.7
20-30%	559	186.4
30-40%	322	129.3
40-50%	173	85.6
50-60%	85.1	53.0
60-70%	37.9	30.1
70-80%	15.1	15.1

Table 2.1: The average number of binary collisions and number of participants estimated by the Glauber Monte Carlo model [17].

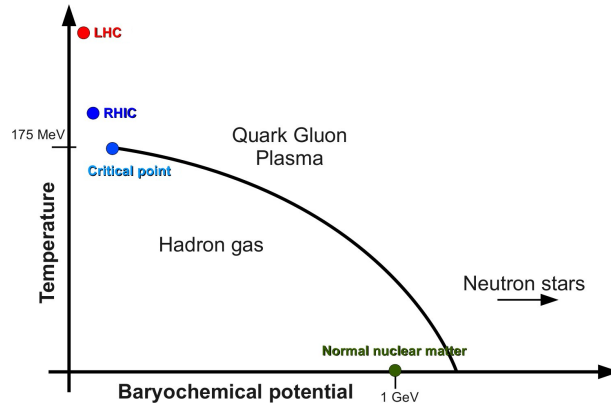


Figure 2.7: Phase diagram for nuclear matter.

2.7 Quark-gluon plasma

In most if not all of our current universe coloured particles are subject to confinement, which is the restriction of quarks to packages of colourless combinations called hadrons. From three colours (and three anti-colours) combinations can be formed that consist of either two quarks, a quark-antiquark pair called a meson, or three quarks (or antiquarks) called baryons. Colourless combinations of more than three quarks have not yet been observed. It was hypothesized in the 1970's [?] that a phase transition might occur if nuclear matter was subjected to extreme temperature and/or energy density, creating a new matter where quarks and gluons would be deconfined. In collider experiments the critical energy density $\epsilon_C \sim 1 \text{ GeV}/\text{fm}^3$ (an order of magnitude higher than in normal nuclear matter) and the associated critical temperature $T_C \sim 170 \text{ MeV}$ could be reached with heavy ions colliding with high enough center of mass energy. The border of the phase transition is shown in Figure 2.7. The indications of a new matter were first signaled at SPS, but finally proven at the RHIC, where gold ions were accelerated to $\sqrt{s_{NN}} = 130 \text{ GeV}$ [18]. The new matter formed at collision point evolves through several stages.

Initial stage ($\tau < 0$). Two heavy ion move towards each other, strongly Lorentz contracted close to the speed of light. Due to the Lorentz contraction a Color Glass Condensate (CGC) is formed, a saturation of gluons in the nucleus.

Pre-equilibrium stage and thermalization ($\tau \lesssim 0.1 \text{ fm}/c$). The first moments after the impact the excited QCD medium takes time to achieve local thermalization. During this first stage particles with high mass and/or large transverse momentum are formed, so-called Hard Probes, such as are heavy quark pairs ($c\bar{c}$ and $b\bar{b}$), weak bosons (Z and W^\pm) or very energetic gluons or quarks that form jets during hadronization.

QGP expansion and hadronization ($\tau \lesssim 10 \text{ fm}/c$). The QGP in equilibrium seems to be governed by hydrodynamic laws describing a perfect liquid. Particles sensitive to the strong force undergo interaction with the medium. During the expan-

sion hadronization takes place at the border of the matter, until the entire medium is converted in hadrons.

Hadronic expansion and decoupling ($\tau \lesssim 20 fm/c$). The hadronic avalanche from the border of the medium expands and decouples from the system.

The stages of the QGP evolution are not yet completely understood. However there are several signatures of the QGP that can be studied, sometimes isolating a specific stage, that are useful to make comparisons to model predictions.

2.8 QGP signatures

The main goal of the HI program is to discover the properties of the QGP such as its equation of state (EoS), temperature, order of phase transition, transport coefficient etc. Several measurements to achieve this have been proposed including collective flow, strangeness enhancement, charmonium suppression, jet quenching and more.

2.8.1 Flow

It was mentioned in the description of the evolution of the QGP that the medium can be described as a perfect liquid. This includes a collective flow of particles along pressure gradients, which results in the emission of more particles in the direction of the largest pressure gradients. These can give insight in the EoS. Several types of flow can be distinguished:

Longitudinal flow, describing the collective motion of particles in the beam direction

Radial flow, describing particles emitted from source with a common velocity field independent of direction

Transverse flow, when the velocity field is independent of the azimuthal angle

Elliptic flow, describing the emission pattern which has a preferential direction with respect to a certain azimuthal angle.

Radial flow is azimuthally averaged and receives contributions from all expansion stages. Elliptic flow is generated mostly during the early stages of the QGP, providing a way to help understand the thermalization and EoS of the QGP.

The observed azimuthal flow can be expressed as a Fourier series in azimuthal angle ϕ [19]:

$$\begin{aligned} E \frac{d^3N}{dp^3} &= \frac{d^2N}{2\pi p_T dp_T d\eta} \left(1 + 2 \sum_{n=1}^{\infty} v_n(p_T, \eta) \cos(\phi - \Phi_n) \right), \\ v_n &= \langle \cos n(\phi - \Phi_n) \rangle, \end{aligned} \quad (2.18)$$

where $\frac{dN}{p_T dp_T d\eta}$ is the pseudorapidity (η) distribution of the transverse momentum (p_T) dependent hadron spectra. v_n and Φ_n represent the magnitude and direction of the

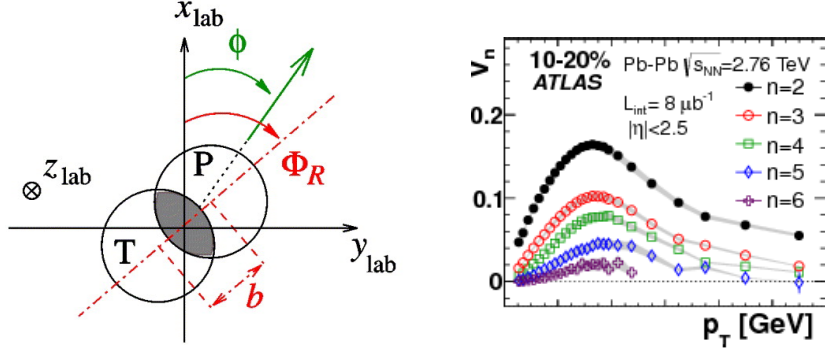


Figure 2.8: *Left*: Event plane geometry showing the orientation of the reaction plane Φ_R [?]. The pressure gradients are strongest along the short axis of the elliptical shape of the overlap area. *Right*: v_n dependence of p_T .

n^{th} -order harmonic, respectively. The n^{th} -order harmonic has n -fold periodicity in the azimuth. At low p_T , the first harmonics are known as *directed flow* v_1 , *elliptic flow* v_2 , or *triangular flow* v_3 . Large values of v_2 are associated to the behaviour of the QGP as a perfect liquid, as it requires a hydrodynamical models with a shear viscosity to energy density ratio. But furthermore v_2 can help to distinguish between different models of the initial geometry and give information on initial state fluctuations.

2.8.2 Jet quenching

It has been seen that high transverse momentum muons are suppressed at rates up to a factor 5 lower than expected assuming QCD factorization holds in every binary collision. This measurement is characterized by the ratio of the yield in Pb+Pb with p+p divided by the number called binary collisions, called the nuclear suppression factor

$$R_{AA} = \frac{1}{N_{\text{coll}}} \frac{d^2 N_{A+A}/dydp_T}{d^2 N_{p+p}/dydp_T}. \quad (2.19)$$

The suppression is the result of interactions and energy loss of particles in the dense medium. As shown in Figure 2.9 the suppression in central collisions is stronger than the suppression in peripheral collisions, due to the higher energy density and temperature in central collisions, as well as a longer average path length for particles traversing the medium.

Another, but similar effect is the modification of jet properties. In proton collisions jets are often formed, with similar energies in a back-to-back fashion. The modification of back-to-back jet energies is a measurable with a jet asymmetry observable

$$A_J = \frac{E_{T1} - E_{T2}}{E_{T1} + E_{T2}}, \quad \Delta\phi > \frac{\pi}{2}. \quad (2.20)$$

The jet asymmetry is plotted on the right in Figure 2.9 for central lead-lead events measured in the ATLAS detector. Although the effects of the medium are clearly visible, the underlying mechanism of in-medium modification is clouded due its effect on both

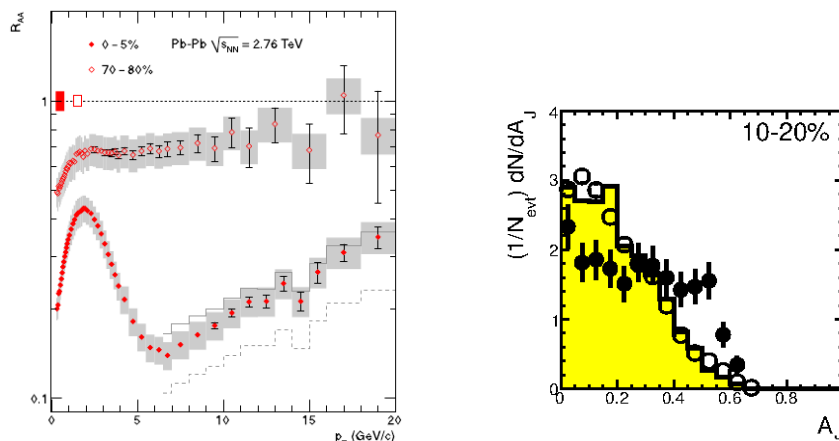


Figure 2.9: *Left:* Suppression of particle spectra as a function of p_T measured by ALICE. Suppression is strong in central events, while for peripheral events the spectra are more similar to QCD factorization expectations [20]. *Right:* Jet asymmetry in central heavy ion collisions (solid black) compared to p+p data (empty circles) and simulation without in-medium particle modification (yellow bars).

jets. A more ideal situation would be one where the exact direction and energy of the parton resulting in a modified jet are known. This is possible if the jet is produced back-to-back in association with a weak boson like in Figure 2.1, if the decay particles of the boson don't interact with the medium, as is the case with decay to leptons. With the energy and the direction of the high p_T parton known, the effect of the medium on the measured jet can be studied more precisely.

Chapter 3

The ATLAS experiment

This chapter will give a very short introduction to the LHC before moving on to the more relevant details of the ATLAS experiment which concern the subject of this thesis.

3.1 Large Hadron Collider

The Large Hadron Collider (LHC) is an accelerator facility built in the tunnel of the preceding Large Electron-Positron Collider (LEP) which was in operation from 1989 until 2000. The LHC, which started operation in 2008, can accelerate protons and heavy ions at unprecedented energies. The design capabilities reach up to a maximum center of mass energy of $\sqrt{s} = 14$ TeV for protons and a nucleon-nucleon center of mass energy for lead nuclei of $\sqrt{s} = 5.52$ TeV. This energy has not yet been reached. Following construction errors that caused considerable damage to the LHC shortly after its startup in 2008, the machine has accelerated up to half the design energies, from 2009 to 2011. In 2012 the beam energy was increased by 1 TeV to $\sqrt{s} = 8$ TeV for the proton-proton run.

Figure 3.1 shows a schematic overview of the accelerator complex at CERN. The LHC can only take in particles at some minimal energy. Protons and heavy ions have to go through several stages, largely made up of repurposed CERN accelerator experiments, before being inserted in the beam pipe. Protons are inserted in the linear LINAC 2, which accelerates protons to 50 MeV, after which there are inserted in the Proton Synchrotron Booster (not pictured), where they are further accelerated to 26 GeV before being inserted in the Proton Synchrotron (PS). PS delivers protons at 26 GeV to the Super Proton Synchrotron (SPS) from where the protons are finally injected in the LHC at 450 GeV beam energy. The first few stages are different for the lead nuclei. These are inserted in LINAC 3 from where they go into the Low-Energy Ion Ring (LEIR) which is used as an ion storage and cooling unit. From LEIR they are injected into the PS from where they follow the same trajectory as the protons.

Four main experiments at the LHC (ATLAS, ALICE, CMS and LHCb) have a detector placed at Interaction Points along the ring.

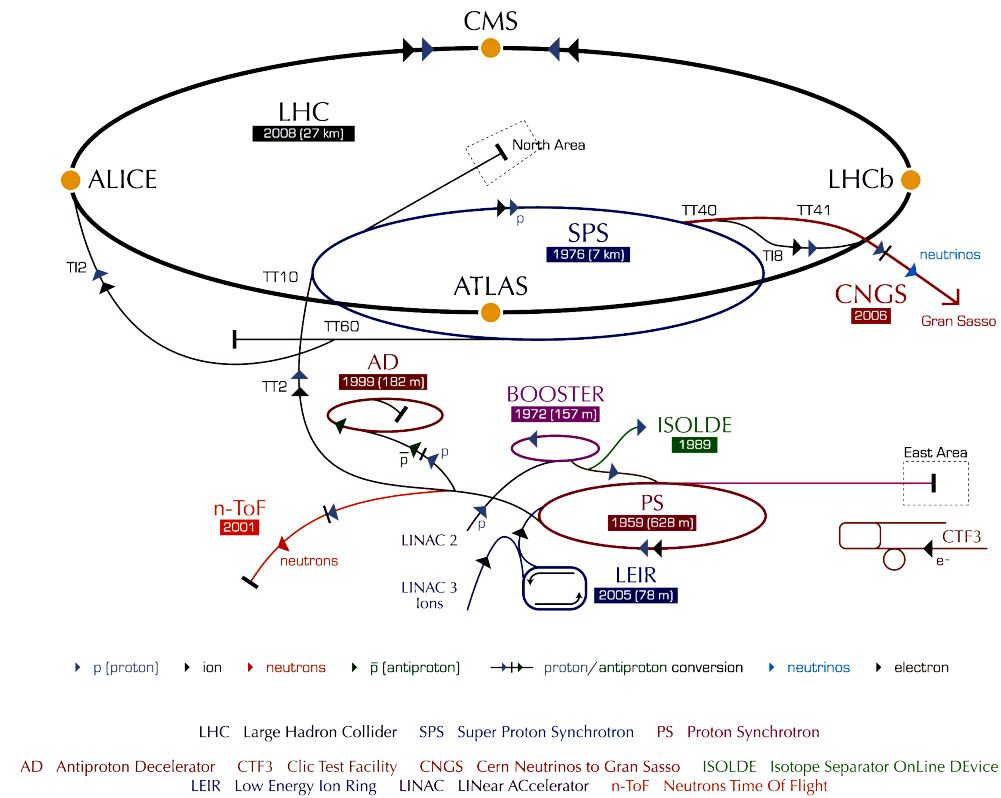


Figure 3.1: CERN's accelerator complex.

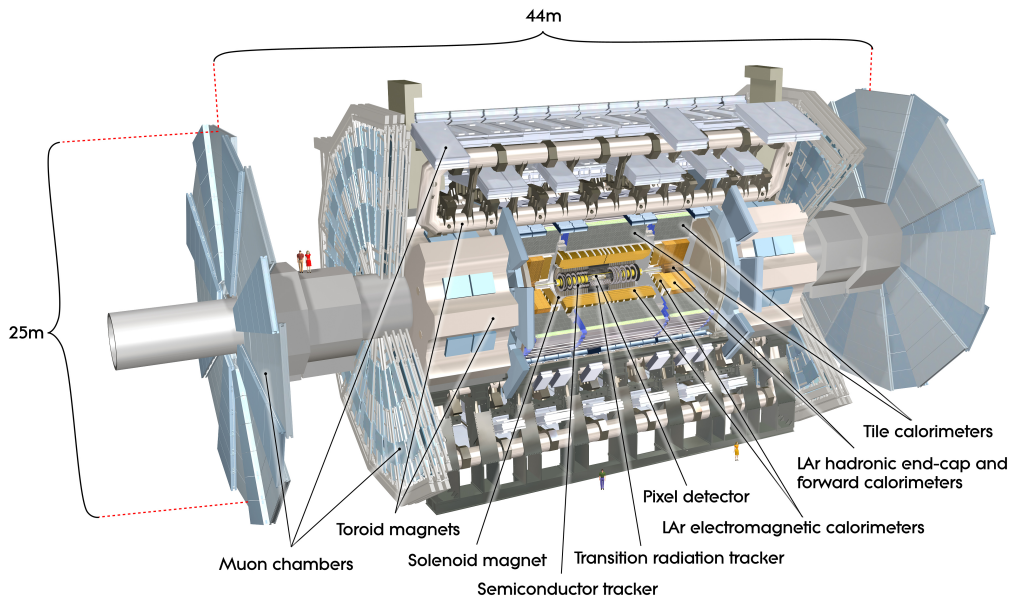


Figure 3.2: Overview of the ATLAS detector.

3.2 ATLAS detector

The ATLAS detector is a forward-backward symmetric detector with respect to the interaction point. The detector consists of three main subdetectors.

- Inner detector (ID). The center of the detector is made up of the ID. As can be seen in Figure 3.2, the ID consists of a pixel detector, semiconductor tracker and transition radiation tracker immersed in a 2 T solenoidal field. The tracking provides pattern recognition, momentum and vertex measurements.
- Calorimeters. Around the ID sit high granularity liquid-argon (LAr) electromagnetic sampling calorimeters which provide energy and position measurements within the pseudorapidity range $|\eta| < 3.2$. Hadronic scintillator-tile calorimeters range up to $|\eta| < 1.7$, but is extended in the end-caps to match the outer $|\eta|$ limits of the end-cap electromagnetic calorimeters. The LAr forward electromagnetic and hadronic calorimeters (FCal) extend pseudorapidity coverage to $|\eta| = 4.9$.
- Muon spectrometer (MS). The only particles likely to make it through the calorimeters are muons (and neutrinos). These are detected by the MS, which surrounds the calorimeter. An air-core toroid system generates bending power and three layers of high precision tracking chambers measure muons passing through. The MS contains special trigger chambers for fast decision making on potentially interesting events.

Aside from these detector elements, the system must be able to use intelligent decision making and provide fast readout. The triggers, initially designed for proton-proton interactions, enable to take informed decisions in the necessary reduction of approximately 1 GHz of interactions at design luminosity ($10^{34} \text{ cm}^{-2} \text{ s}^{-1}$) to the 200 Hz maximum rate acceptable for data recording. The trigger system is built up in three levels. The Level-1 (L1) trigger scans a subset of detector information to decide whether or not to reject the event, reducing the data rate to approximately 75 kHz. Two subsequent triggers, Level-2 (L2) and the event filter, are called the high-level triggers. Together they bring the data rate down to approximately 200 Hz.

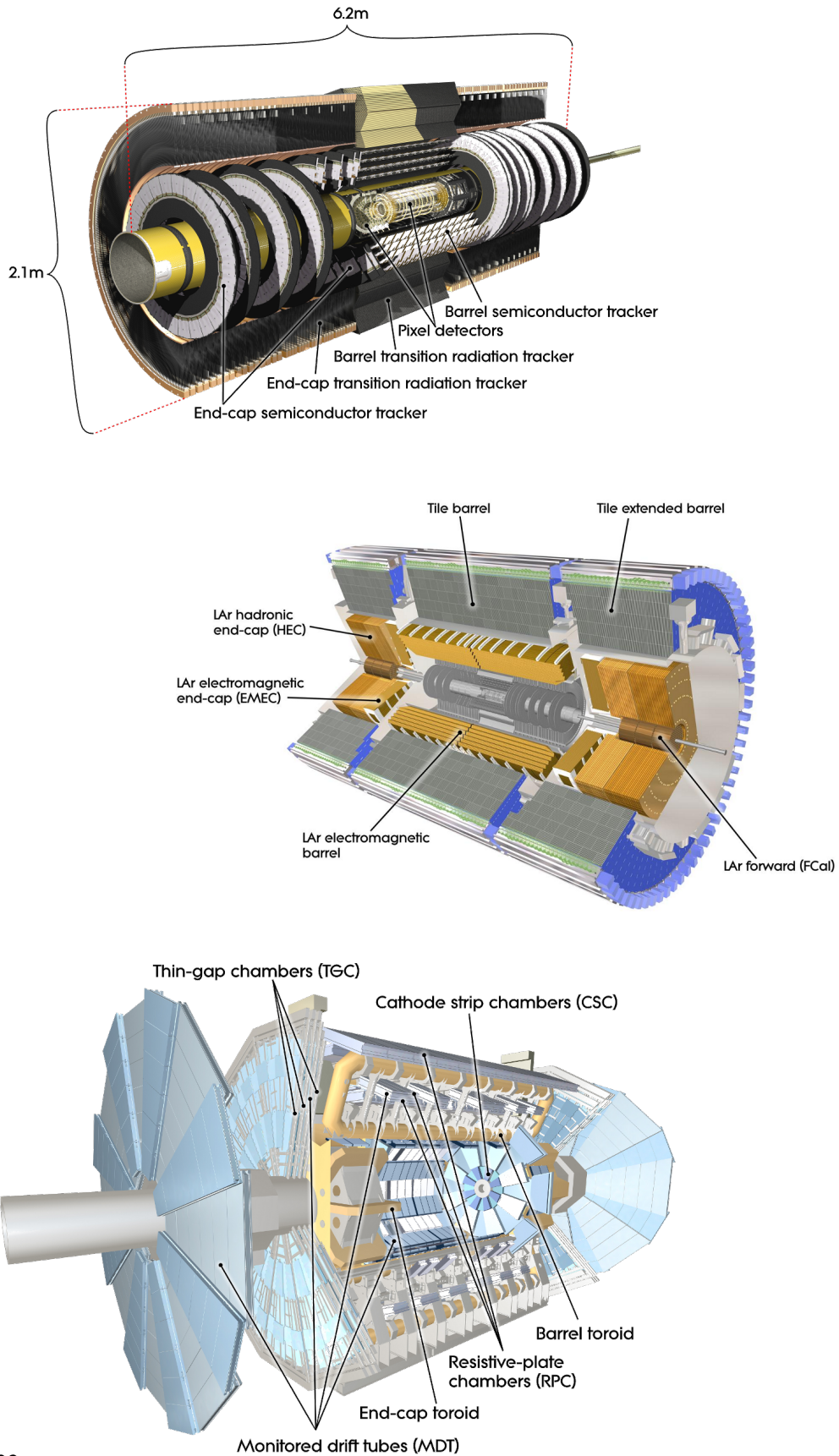


Figure 3.3: *Top:* The Inner Detector (ID). *Middle:* Electro-magnetic and hadronic calorimeters. *Bottom:* The Muon Spectrometer (MS).

3.3 Inner detector

The Inner Detector, designed to provide tracking measurements for charged particles, is placed around the collision point where in heavy ion collisions up to 5000 particles emerge. In proton-proton collisions, operations are slightly less challenging but with approximately 1000 particles still results in a very large track density. To achieve the high-precision measurements required for momentum and vertex reconstruction the detector needs fine granularity. This is provided by the pixel and silicon microstrip trackers (SCT), used in conjunction with the straw tubes of the Transition Radiation Tracker (TRT). The pixel detector provides the highest granularity around the vertex region with a minimum pixel size in $R - \phi \times z$ of $50 \times 400 \mu\text{m}^2$. Particles cross typically three layers of this detector and eight strip layers of the SCT. The stereo strips are positioned in layers at an angle (40 mrad), providing four spacepoints for the measurement. The pixel detector has 80.4 million readout channels while the SCT has 6.3 million.

The TRT consists of 4mm straw tubes, for tracking up to $|\eta| < 2.0$. The tubes are positioned parallel to the beam axis and are 144 cm long. A charged particle typically leaves 36 hits while traversing the TRT, which can be measured with an intrinsic accuracy of $130 \mu\text{m}$ per straw. The TRT has approximately 351,000 readout channels. Despite the low granularity, the momentum measurement is significantly improved due to the extension of the measured track.

During the 2012 heavy ion run, the TRT was suffering from unresponsive areas. Therefore TRT information was not used in track reconstruction. For muons the impact this is very small, as their measurement depends more on the MS.

3.4 Muon spectrometer

Precision measurements in the direction of the muon track coordinates over most of the η range is provided by Monitored Drift Tubes (MDT's) located between and on the eight coils of the superconducting barrel toroid magnet. The drift tubes contain wires which are mechanically isolated. At large rapidities Cathode Strip Chambers (CSC's) with higher granularity cover the range $2 < |\eta| < 2.7$. CSC's consist of multiwire proportional chambers with cathodes segmented into strips. The trigger system, illustrated in Figure 3.4 covers the pseudorapidity range $|\eta| < 2.4$ with Resistive Plate Chambers (RPC's) in the barrel and Thin Gap Chambers (TGC's) in the end-cap regions. Besides their purpose as trigger they improve the muon measurement by measuring the coordinate in the direction orthogonal to the one determined by the precision chambers.

The transverse momentum of the muons can be measured from about 3 TeV down to 3 GeV. At lower transverse momentum, muons at midrapidity are unlikely to punch through the calorimeters.

The performance of the large MS depends on the alignment of the muon chambers with respect to each other and to the rest of the detector. Approximately 12000 alignment sensors monitor deformations and relative positions of the MDT chambers enabling measurements of under $30 \mu\text{m}$. In addition the magnetic field is continuously monitored by approximately 1800 Hall sensors, in order to make correct extrapolations for muon tracks. The alignment accuracy is overestimated in 2011 simulations, leading

to too optimistic muon p_T resolution in the reconstruction. This is corrected for with designated muon momentum smearing code in the analysis.

3.5 Forward detectors

ATLAS has three detectors to cover the forward region. Two of them are mainly used for luminosity measurements but for this analysis the most relevant one is the Zero-Degree Calorimeter (ZDC). It is located at ± 140 m from the interaction point, right before the point where the beam-pipe containing bunches moving in opposite directions is again splitted into two separate one direction beam-pipes. The ZDC modules use layers of alternating quartz rods and tungsten plates to measure neutral particles at pseudorapities $|\eta| \geq 8.2$.

3.6 Triggers

The L1 trigger searches for interesting events using information from a subset of detectors. The high transverse momentum muons are identified by the trigger chambers in the barrel and end-cap regions of the MS while reduced-granularity information from the calorimeters is used for activity there. All L1 information goes to a central trigger processor which takes into account the general trigger menu, a specified set of requirements composed to define an interesting event using available triggers. This includes prescaling of certain triggers (a prescale of 0.5 means that even if the trigger fired, there is a 50% chance this trigger will decide to keep the event). The L1 trigger is used to define Regions-of-Interest (RoI). Full information from the RoI, including the type of feature identified and the criteria passed for L1, is sent to the high-level trigger. This is approximately 2% of total event data. Finally events are passed on to the event filter. Each step reduces the event rate through trigger requirements and prescales.

3.7 Muon reconstruction algorithms and track fitting

The muon reconstruction is based on digitized information from the detectors. Several algorithms are designed for various reconstruction aspects, e.g. pattern recognition, track fitting, vertex determination and energy measurements.

Detector information is used to reconstruct muons that can be categorized in four types, called combined, stand-alone, segment tagged and calorimeter tagged muons.

- **Combined muon.** Muons are charged particles that leave a track in the ID and in the designated MS. Combining information from the ID and the MS provides maximal parameters for a global fit, which result in a optimal momentum and vertex resolution. If a track in MS is successfully combined with a track in the ID to perform a global fit, a combined muons is made.

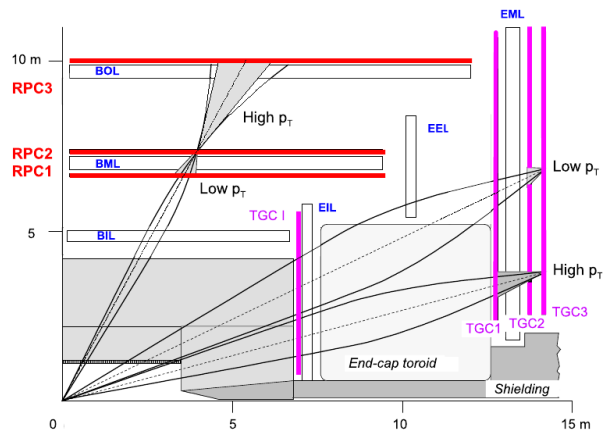


Figure 3.4: Schematic of the muon trigger system. In blue letters (BIL, EML etc.) is shown the MDT chambers, which are the precision detectors not used for the trigger. The trigger dedicated detectors are placed close to the MDT's, in magenta the TGC (end-cap) and in red the RPC (barrel).

- Stand-alone muon. For MS tracks that are not combined with ID tracks, reconstruction is based on MS information only. From an extrapolated track back to the beam line the muon properties are calculated.
- Segment tagged muon. If an ID track can be extrapolated to straight line segments in the MS, but the MS does not have a complete track, a segment tagged muon is made.
- Calorimeter tagged muon. An ID track associated to an energy deposition in the calorimeter compatible with the hypothesis of a minimum ionizing particle, but not associated to a track in the MS makes a calorimeter tagged muon. These muon candidates are usually low transverse momentum muons. They are not used in heavy ion reconstruction.

Many algorithms contribute to the formation of these types of muon candidates and they are continuously under development. The oversight given here will reflect the status existing during the analysis.

The muon reconstruction algorithms are divided in two so-called "chains", called MUID and STACO. The chains are formed by two sets of algorithms applied separately for reconstruction. The MUID chain consists of the following algorithms:

- Moore and Muid Standalone. Moore uses hit information in the MS to produce standalone segments and tracks. Muid Standalone extrapolates the Moore track to the vertex and uses a vertex constraint to determine the track parameters at the vertex. Muid Standalone outputs the muon properties at the vertex.
- Muid Combined. Produces combined muons by performing a global refit of a MS track combined with an ID track.

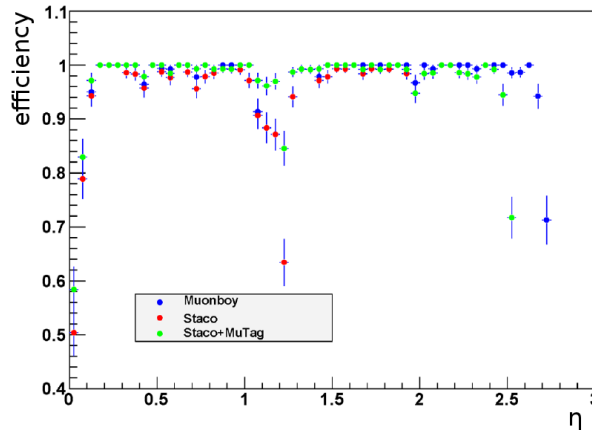


Figure 3.5: STACO algorithm efficiencies as a function of pseudo-rapidity η for the Muonboy (blue), Staco (red) and the MuTag+Staco (green) algorithms from a simulation with 100 p_T muons [21].

- MuGirl. Starts from an ID track and performs a search for associated segments and tracks in the MS. If a full track refit is possible a combined muon is made. Otherwise a tagged muon is made.
- MuTagIMO. Tries to associate ID tracks to Inner-Middle-Outer Moore segments and produces a tagged muon.

STACO is built up in a similar fashion but with different algorithms:

- Muonboy. Uses hit information in MS to produce segments and tracks which are extrapolated to the vertex.
- Staco combines an ID track with a MS track using a statistical method to produce combined muons.
- MuTag. Associates ID track to Muonboy segments if the MS and/or ID track were not already used by the Staco algorithm. In this case a tagged muon is made.

The algorithms in the MUID and STACO chains are applied separately to reconstruct muon candidates, and many muons will be reconstructed by several of them. Overlap in muon candidates within the chains is removed when data analysis files are processed. As seen in Figure 3.5, the muon reconstruction algorithms have varying efficiencies. The chains combine several algorithms to achieve higher efficiency, the STACO and MUID chains however remain separate. At the analysis level they will be merged as described in Section 4.2.1. A more optimal scenario where STACO and MUID algorithms are combined at the reconstruction level was not available during analysis, however development was under way.

In general, from pattern recognition to muon property reconstruction the following steps are identified:

-
- Hits in the various MS stations form track segments. Each segment is extrapolated based on an initial rough estimate of the muon p_T to find associated muon track segments. If several segments are associated, a candidate track is formed and used for a fit to extract a more accurate estimate of the momentum, position and direction.
 - A new global fit is performed from the raw information from the stations in stead of the loose segments. This procedure removes "bad" hits from the fit.
 - A new fit is made including energy loss and multiple scattering effects. The most probable energy loss is parametrized as a function of the momentum and the amount of matter crossed, and is applied at the scattering points.

The Staco and Muid Combined algorithms both attempt to combine ID and MS tracks for a full muon property reconstruction but their approach differs slightly. Muid Combined makes a global refit of the hits in the ID and MS, while Staco makes a statistical combination of both independent fits in the subdetectors [?].

For high p_T muons, for example for Z decay products, the ATLAS detector delivers excellent reconstruction efficiency of $> 96\%$. Both algorithms define muons as "loose", "medium" and "tight", the same definitions in both algorithms are not equivalent. The definition of "tight" muon is given in Table 3.1. The "tight" definition requires a com-

MUID	Combined Muon
	Standalone muon with $ \eta > 2.5$ and 3 MDT+CSC stations
	MuGirl with extended track with number of MDT+CSC stations > 2
	MuGirl with extended track with number of MDT+CSC holes < 6
STACO	Combined Muon
	MuTag candidate with at least 3 TGC Phi hits in tagging segments
	MuTag candidate with at least 2 tagging segments

Table 3.1: Tight definitions for MUID and STACO.

bination of MS and ID information where possible and are generally used in analysis.

Chapter 4

Analysis

4.1 ATLAS data and stability

4.1.1 Data and event selection

During the 2011 heavy ion running of the LHC the ATLAS detector recorded data in four different non-overlapping physics streams.

- **Hard Probes stream.** A special trigger menu consisting of muon and calorimeter triggers was used to filter events with high transverse momentum (p_T) jets, photons, electrons and muons. The di-muon triggers (in principle good for Z boson analysis) were found to have less than optimal efficiency, in stead single muon triggers were used. The data taking bandwidth was sufficient to allow the muon triggers to run without prescale. The Hard Probes stream collected a data sample corresponding to an integrated luminosity of $158 \mu\text{b}^{-1}$. A Good Run List, a register that states whether the detector was fully functioning during data taking reduces the analysed luminosity to $142 \mu\text{b}^{-1}$. The total number of events in the sample is 60.8 million.
- **Minimum Bias stream.** Another set of triggers (MBTS, ZDC described later) is used to take data with little or no bias. The Minimum Bias data taking rate was set to complement the unprescaled Hard Probes stream for maximal bandwidth. Over the 2011 run the effective prescale was 15.6. The MB stream contains 68.7 million events.
- **Ultra-peripheral stream.** A selection of events aimed at recording photo-nuclear events. These events are not recorded by the HP or MB stream, and are 2-3 times smaller than the MB events. The UP stream contains 7.3 million events. This stream is not used in the analysis.
- **Overlay stream.** A selection of MB events without zero suppression was recorded for future overlay with PYTHIA. The overlay was not fully ready and understood for this analysis.

Selection of MB events was performed using a trigger for a transverse energy calorimeter deposition of 50 GeV with a complementary ZDC trigger for events with lower calorimeter deposition. Additionally the Minimum Bias Trigger Scintillators (MBTS) were required to fire within 3 ns of each other on opposite sides of the interaction region. Finally a MB event was required to have a reconstructed primary vertex within 150 mm of the nominal ATLAS centre.

For the $Z \rightarrow \mu^+\mu^-$ analysis the Hard Probes stream was used, with events also satisfying the MB event selection and the GRL.

In the analysis results are presented sometimes as per event counts. For this the luminosity is converted into number of events using the Pb+Pb full cross section of 7.1 b. The MB fraction of all inelastic events is $98 \pm 2\%$. The equivalent number of MB events for the HP analysis is thus $(1.010 \pm 0.02) \times 10^9$.

4.1.2 Centrality association in data

Event centrality is determined with the total transverse energy ($\sum E_T$) measured by the FCal detector [?]. For each centrality class the geometric event characteristics and their systematic uncertainties were based on the Glauber model (Section 2.5) and a match of it to the FCal $\sum E_T$ distribution. Table 4.1 lists the energy deposition associated to a

Centrality	FCal $\sum E_T$ [TeV]	N_{part}		N_{coll}	
0-5%	3.8000-2.8038	382.2±2.0	0.5%	1683.±130.	7.7%
5-10%	2.8038-2.3102	330.3±3.0	0.9%	1318.±99.0	7.5%
10-20%	2.3102-1.5707	260.7±3.5	1.4%	923.3±68.3	7.4%
20-40%	1.5707-0.6624	157.8±3.9	2.5%	440.6±32.2	7.3%
40-80%	0.6624-0.0438	45.9±2.8	6.0%	77.8±7.3	9.4%

Table 4.1: Centrality, 2011 FCal cuts and MC Glauber parameters used in the analysis.

certain centrality class, with the MC Glauber parameters N_{part} and N_{coll} with uncertainties included on the right.

The MB event centrality distribution was checked against Table 4.1 with Figure 4.1, showing on the left the number of events per 1% in centrality classes 0 to 8, corresponding to 0-5%, 5-10%, 10-20%...70-80%. It demonstrates a flat distribution with a non significant residual deviation of approximately 1%. Shown in the right panel of Figure 4.1 is the pile-up fraction estimated by convolution of the MB FCal distribution with itself and matching to data above $\sum E_T = 4$ GeV. At $E_T > 4.0$ TeV all events are identified as pile-up. A cut of 3.8 TeV was used to keep pile-up negligible in the most highest centrality class.

4.1.3 Run-by-run stability

In order to make reliable physics statements it is important to verify that the detector was functioning as expected during data taking. If detector components were display-

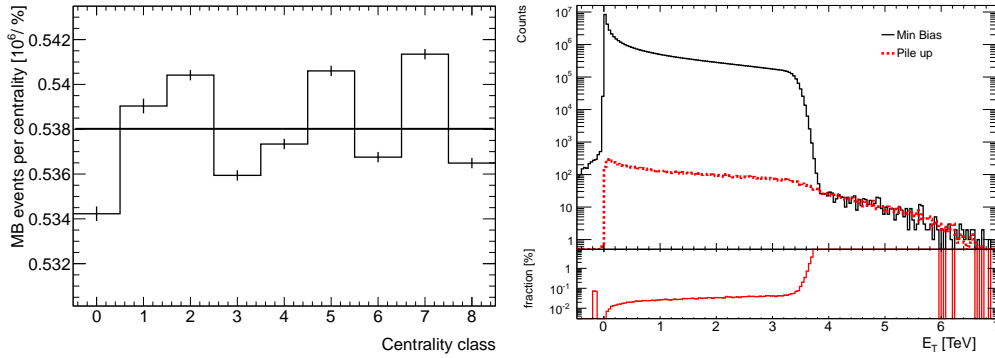


Figure 4.1: Left: Number of MB events per 1% of centrality. Right: estimate of the pileup (red) events in the MB (black) sample. Low panel shows the pileup fraction.

ing problems during run time, the events recorded during that time are registered in the Good Run List (GRL). These events are excluded in the analysis. Additional checks at an analysis level make sure that for the remaining events, the detector readout was stable throughout the run. Figure 4.2 shows the per event yield for various observables, scaled down in order to display them in the same frame. The number of tracks reconstructed in the ID before cuts is shown in green. The MUID and STACO lines show the average number of muons for the respective reconstruction chains in red and blue. ECal E_T for the barrel end FCal E_T for the forward calorimeters are the E_T in corresponding detectors. Since centrality determination is an important for analysis results, FCal stability is crucial. The figure displays very stable run condition throughout the 2011 run. The first point, due to a disfunctioning MB trigger, shows erroneous behaviour and was excluded in the analysis.

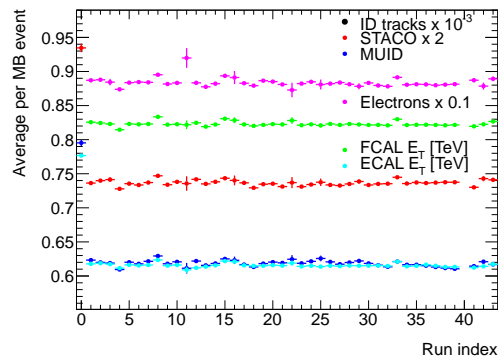


Figure 4.2: Average over the run values for several parameters used in the analysis plotted vs. run index.

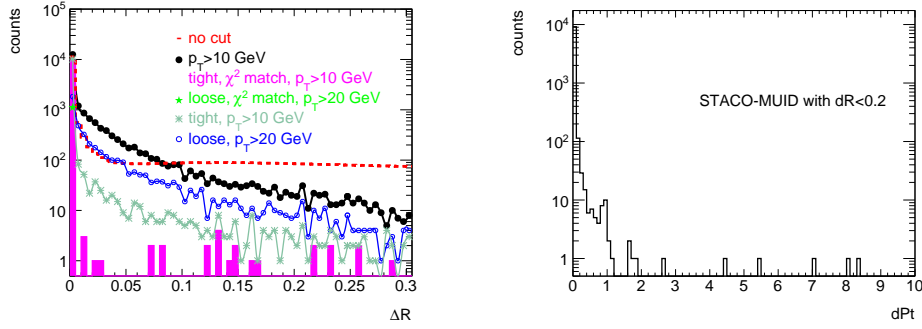


Figure 4.3: *Left*: ΔR between MUID and STACO muons for different muon quality selections. ‘No cut’ histogram is scaled down. *Right*: $\frac{p_T^{MUID} - p_T^{STACO}}{p_T^{MUID}}$ distribution for muons with $\Delta R < 0.2$, plotted from Monte Carlo.

4.2 Single muon reconstruction

4.2.1 Merging

The ATLAS reconstruction software provides two main reconstruction strategies (MUID and STACO) as described in Section 3.7. Although for physics analysis it is usually advised to use muons reconstructed through one of these strategies, the limited statistics in this analysis are a motivation to optimize reconstruction efficiency where possible. Therefore both reconstruction strategies are exploited by merging muons from the two channels to form a new muon sample. The procedure used is described here.

The main issue in the merging process is to prevent duplicates (muons reconstructed with overlapping hits in the detector) entering the analysis. This is done on a physics level by looking the properties of the reconstructed muon. In case of an identified duplicate, the quality of reconstruction is used to decide whether to use a STACO or MUID muon in the analysis.

The first step is for each event the MUID muon container is copied in its entirety. Muons in the STACO container are then one by one compared to muons in the MUID container to identify duplicates. Muons are considered duplicates if the STACO muon is associated to a MUID muon with the following properties:

$$\Delta R (\sqrt{\Delta\phi^2 + \Delta\eta^2}) < 0.2$$

$$\Delta p_T (\frac{p_T^{MUID} - p_T^{STACO}}{p_T^{MUID}}) < 0.4$$

Here ΔR is the radial distance between the STACO and MUID muon, and Δp_T is the relative difference between the p_T of the muons. The left of Figure 4.3 shows the distribution of the radial distance of the muons. Based on the shape for muons with $p_T > 10$ GeV (continuous black line) a cut value of 0.2 was determined. The second parameter Δp_T is shown in the right figure, for muons which pass the first condition. A condition of 0.4 is applied to allow muons with very different p_T but reconstructed very close to each other to both be considered for analysis. If a STACO muon does not pass these requirements

with respect to one of the MUID muons, it is included in the new merged muon container. A STACO muon passing these conditions is considered a reconstruction of the same physical muon. The quality of reconstruction is consequently used as a parameter to decide whether to pass on the STACO or MUID muon to the merged container. This decision is based on the following conditions with increasing hierarchical importance.

$$|d_0|, |z_0 \sin(\theta)| < 50 \text{ mm}$$

tight

$$\text{match } \chi^2/n_{\text{dof}} \leq 10$$

The d_0 and z_0 condition are a loose requirement on the muon track to point to the vertex. The definition of *tight* is detailed in 3.7. The match is a reflection of the quality of the fit between the Muon Spectrometer (MS) track and Inner Detector (ID) track. The muon that passes most requirements is passed on to the merged container. If a STACO and MUID muon are considered of equal reconstruction quality, the MUID muon is used. This is done because MUID in general has a slightly better momentum resolution. Figure 4.4 shows that with the procedure described above a reconstruction efficiency is achieved with an approximately 1% increase in efficiency with respect to the most efficient default algorithms.

The effectiveness of the procedure demonstrates the muon reconstruction in ATLAS can and should be improved. In fact, during this analysis a new muon chain was written which does better employ the available reconstruction algorithms to achieve higher efficiencies. Unfortunately the new chain was not ready for this analysis but is as of this date, rendering the procedure outlined here and the MUID and STACO chains themselves obsolete.

4.2.2 Simulation

In order to correct for reconstruction efficiency, cut efficiency and acceptance, a Monte Carlo sample of PYTHIA embedded in HIJING was used. PYTHIA is a generator

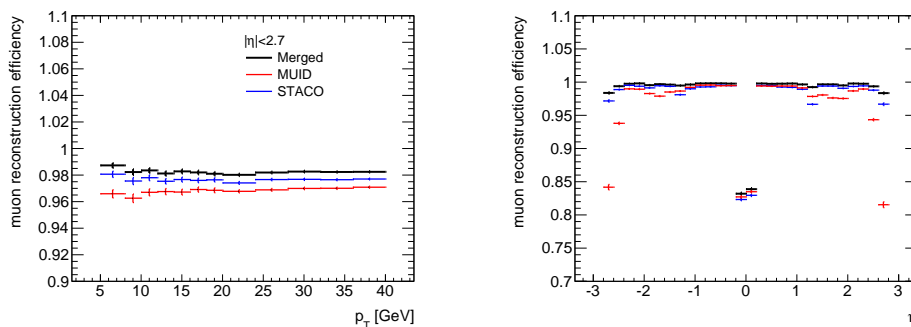


Figure 4.4: *Left*: Muon reconstruction efficiency as a function of the generated p_T . *Right*: The same as a function of η . Merging MUID (in red) and STACO (in blue) yields a higher efficiency (in black.)

which can be used to simulate Z -kinematics in nucleon-nucleon collisions, as well as the kinematics of given decay products, in this case muons. HIJING provides for the simulation of the wealth of particles created in Heavy Ion collisions. Its purpose is to create a similar environment for among which the Z s produced and decays, so that several detector effects affected by multiplicity is correctly taken into account. The detector response is simulated by a program called GEANT4, which contains a complete description of detector geometry and materials. Other programs simulate the digitization of the signal. The digitized signal is then processed in exactly the same manner as real data, using the same software and reconstruction framework.

Properties of reconstructed particles in the processed simulation have to be associated to the truth information, i.e. the input for the GEANT4, so detector response and efficiencies can be studied. In this case, the interest is in the muons. A muon truth matching is by default present in the ATLAS reconstruction data file, the exact details of which are not discussed here. The method used has a serious shortcoming however, as it associates generated muons to reconstructed muons through the properties of ID tracks. This excludes a considerable fraction of muons which are only reconstructed in the Muon Spectrometer from being matched to truth, even though these muons are relevant for the analysis. For that reason additional matching was applied for Stand Alone muons. This was done using the radial distance ($\Delta R = \sqrt{\Delta\phi^2 + \Delta\eta^2}$) of the reconstructed muon to the generated muon. The ΔR distribution is shown in the left plot of Figure 4.5. The figure shows the radial distance from generated to reconstructed muon for muons with the same charge (red line), and for a muon reconstructed with opposite charge (blue line). This visualises the separation between random matching and real matching. A small rise of the blue line towards the y -axis indicates a small amount of charge swapping in the muon reconstruction. Based on the separation between equal and opposite sign matching, an effective value for ΔR was further studied in the plot on the right side of Figure 4.5. Shown here is the reconstructed mass spectrum of muon pairs for which the muons are matched to truth with a ΔR value between 0.1 and 0.2 (continuous line), as well as between 0.2 and 0.3 (dashed line). While the gain of the first is considerable, the second shows a tiny signal in the data region and a similar amount reconstructed in the low mass region, which is the result of random matches to truth. Based on this information a conesize of $\Delta R < 0.2$ is used in the analysis.

4.2.3 Muon reconstruction efficiency

With the simulated $Z \rightarrow \mu^+ \mu^-$ events the efficiency of the detector system can be studied. Figure 4.6 shows the reconstruction efficiency for muons reconstructed in the MS as well as for muons reconstructed in the MS with an associated ID track. An acceptance cut of $\eta < 2.7$ is included for the left plot and a momentum cut of $p_T > 5$ GeV for the right hand plot to show the efficiency in optimal conditions. The efficiency of the MS in rapidities below 2.5 and for muon with $p_T > 5$ GeV show the MS is a very capable muon detector with an efficiency near 100%. The efficiency for central events is in the approximately 1-2% lower. If in addition a track in the ID is required the efficiency is around 90%. The ID track requirements adds to the discrepancy between the centrality classes. Further details on the reconstruction and selection efficiency are studied in the

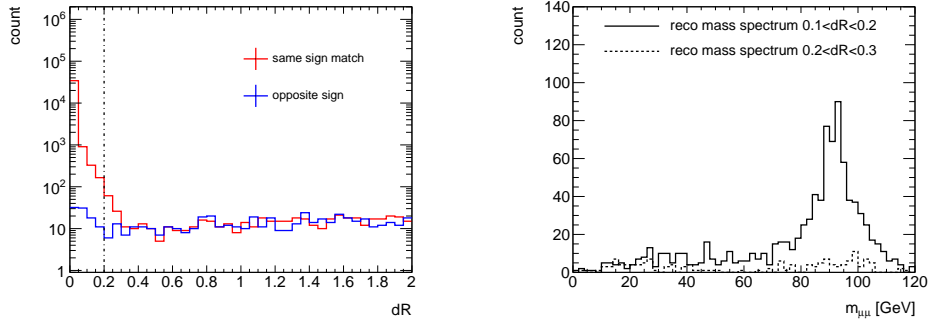


Figure 4.5: On the left is shown the radial distance of generated to stand alone reconstructed muons, where only the smallest distance to one of the muons is plotted. The cut for matching the stand alone muons is set to 0.2. On the right is shown the invariant mass of matched muon pairs with conesize between 0.1 and 0.2, and between 0.2 and 0.3.

next section.

4.2.4 Muon trigger and selection efficiency

This analysis uses the Hard Probes data, which is data recorded with triggers that are tuned for specific physics interest. Among these triggers are the muon triggers which are used for this analysis. However triggers are not ideal and suffer from inefficiencies which can be momentum, rapidity and centrality dependent. This would create a bias in the data sample that, for many physics interests, has to be corrected for. This is done with data recorded in the Minimum Bias stream where events passing the Minimum Bias trigger are recorded. The triggers used for the Hard Probes stream are active here but not used in the decision to keep the event, hence the efficiency of the triggers can

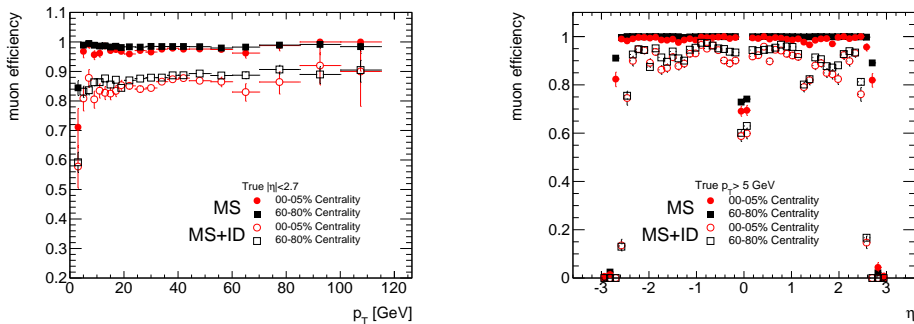


Figure 4.6: The figures show the single muon reconstruction efficiency in p_T and η from PYTHIA $Z \rightarrow \mu^+ \mu^-$ embedded into HIJING for central (0 – 5%) and peripheral (60 – 80%) events. The solid markers show the reconstruction efficiency of muons reconstructed in the MS. The open markers show the efficiency for muons that are in addition associated with a track in the ID.

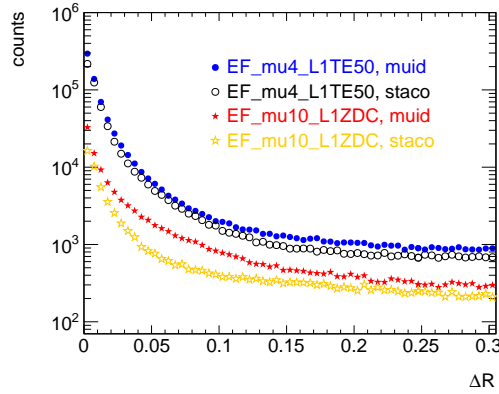


Figure 4.7: *Left:* ΔR distributions used to match online and offline muons for different triggers and reconstruction algorithms.

be checked. The efficiency here is defined as the fraction of reconstructed muons firing the trigger versus all reconstructed muons.. To associate reconstructed muons (offline) to the muon trigger object (online) the radial distance between the muon candidate and the fast online reconstructed object is used. The ΔR distributions for offline to online muons is shown in Figure 4.7. The requirement of the best cone match in $(\eta - \phi)$ space with the condition is $\Delta R = \sqrt{\Delta\phi^2 + \Delta\eta^2} < 0.2$.

$$\epsilon_{trig}^{\mu}(p_T, \eta) = \frac{\left(\text{muon passing the offline selection cuts}\right) \&\& \left(\text{matched to trigger}\right)}{\text{muon passing the offline selection cuts}} \quad (4.1)$$

Figure 4.8 shows the single muon trigger efficiency (ϵ_{trig}^{μ}) for all muon candidates, on the left for the MU4 (for muons with $p_T > 4$ GeV) on the right for MU4 *or* MU10 (for muons with $p_T > 10$ GeV). The strange shape of the efficiency curve results from the presence of fake muons in the muon container. For low reconstruction quality muons, i.e. there are fewer detector parts involved in the reconstruction and/or they have fewer hits, the muon candidate sample becomes contaminated with false muons. These do not fire the trigger system and results in the picture of a misleading low efficiency. However, if a higher reconstruction quality is required, the trigger efficiency will move towards its more realistic value.

A requirement on the ID-MS track match of $\chi^2/n_{dof} \leq 10$ is needed to clean the offline muon sample from fake candidates. The result of this condition is shown in Figure 4.9. The efficiency curve is well described by the fitting error function described in the form:

$$\epsilon_{trig}^{\mu}(p_T) = \epsilon_{trig}^{\text{sat}} \left(1 + \text{erf} \left(\frac{p_T - p_T^{\text{thresh}}}{\text{slope}} \right) \right) \quad (4.2)$$

where p_T^{thresh} , slope and ϵ_{trig} are fit parameters for effective trigger threshold, the turn on slope and the plateau efficiency. The trigger efficiency was studied for centrality and rapidity effects.

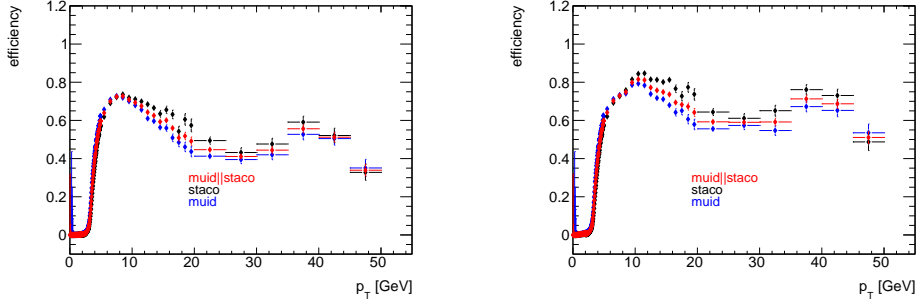


Figure 4.8: $\epsilon_{\text{trig}}^{\mu}(p_{\text{T}})$ for mu4 trigger (left) and mu4 OR mu10 (right). Muons reconstructed exclusively by MUID are shown in blue, STACO in black, and the merged container in red.

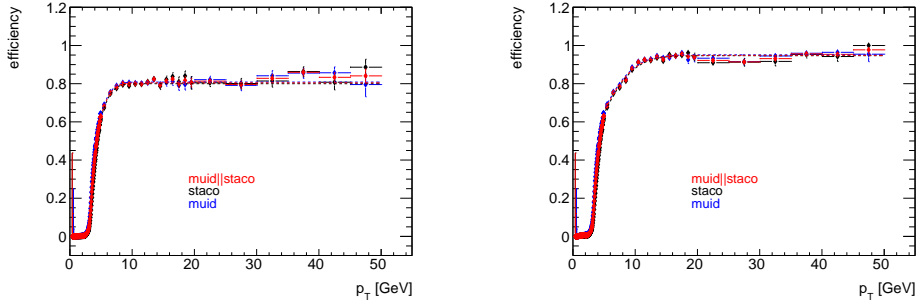


Figure 4.9: *Left*: $\epsilon_{\text{trig}}^{\mu}(p_{\text{T}})$ for MU4 trigger after applying χ^2 matching requirement, shown for the MUID, STACO and merged muon container. The dotted line shows the fit to data as described in the text. *Right*: The same as in the figure on the left but for muons with a MU4 or MU10 trigger match.

In various centrality and rapidity slices the fit function was fitted to data. The plateau value and uncertainty (from the fit) are shown in Table 4.2. A rapidity dependence is observed only in the most central events, while there is a general centrality dependence in the trigger efficiency.

The track match requirement is necessary to be able to correct for trigger efficiency, and is inherently efficient for selecting ‘good muons’ for the Z analysis. However the condition also lowers the overall reconstruction efficiency. In Figure 4.6 was shown that the reconstruction efficiency without quality selection is close to 100%. Figure 4.10 shows the efficiency of different cuts used in the analysis for the most central events. Cut efficiency is defined as the ratio of muons that pass cuts with respect to the muons that are successfully reconstructed. The d_0, z_0 cut is a requirement on vertex pointing of the muons. Z bosons have a very short lifetime and any decay products should point back to the vertex. Outside the region muons are the likely result of decays of particles with longer lifetime or are scattered muons. The integrated single muon cut efficiency for muons with $p_{\text{T}} > 15$ GeV is 89.2%. This number is used to compare with the Tag and Probes method later in Section 4.3.4.

Centrality	$ \eta $	MUID	STACO	Merged
(0-10)%	(0.0-1.2)	92.7 \pm 1.1	94.2 \pm 1.2	93.4 \pm 0.8
	(1.2-2.0)	91.0 \pm 0.8	91.3 \pm 1.0	90.7 \pm 0.6
	(2.0-2.5)	89.3 \pm 2.8	81.2 \pm 2.4	86.1 \pm 2.0
(10-20)%	(0.0-1.2)	96.4 \pm 1.1	98.0 \pm 0.9	97.7 \pm 0.7
	(1.2-2.0)	95.7 \pm 0.6	92.7 \pm 0.8	94.4 \pm 0.5
	(2.0-2.5)	98.0 \pm 3.4	94.8 \pm 3.7	97.5 \pm 2.1
(20-40)%	(0.0-1.2)	99.6 \pm 0.6	100.0 \pm 0.7	99.9 \pm 0.5
	(1.2-2.0)	97.5 \pm 0.5	91.0 \pm 0.8	94.1 \pm 0.5
	(2.0-2.5)	95.9 \pm 2.6	95.1 \pm 2.3	95.4 \pm 1.7
(40-80)%	(0.0-1.2)	98.7 \pm 1.0	98.7 \pm 1.1	98.9 \pm 0.8
	(1.2-2.0)	96.9 \pm 0.9	91.1 \pm 1.4	94.1 \pm 0.8
	(2.0-2.5)	99.3 \pm 3.2	98.8 \pm 4.2	99.9 \pm 2.1

Table 4.2: Single muon trigger efficiency ϵ_{trig}^{μ} [%] at high transverse momentum for the combination of the ‘MU4’ and ‘MU10’ triggers used in the analysis at different centrality and pseudorapidity slices.

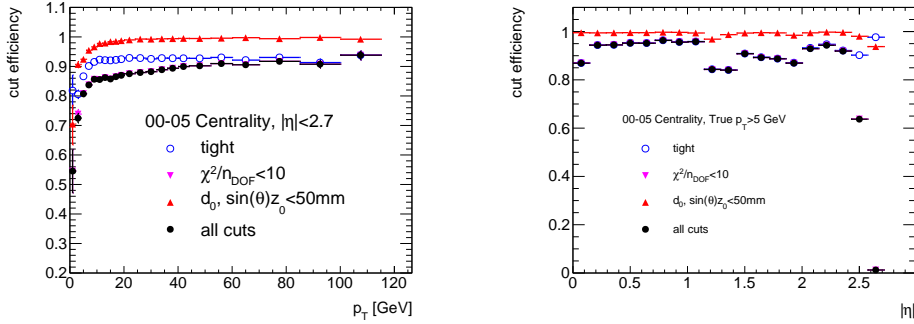


Figure 4.10: *Left*: Muon cut efficiency relative to successfully reconstructed muons as a function of muon p_T for most central events. *Right*: Same as in the left figure versus η .

4.3 $Z \rightarrow \mu^+ \mu^-$ reconstruction

4.3.1 Selection of $Z \rightarrow \mu^+ \mu^-$ -candidates

The procedure for the Z -candidate selection is similar to the one for the single muons. The goal is to maximize the Z reconstruction efficiency while reducing background to the lowest achievable level. Reconstructed muons in an event are paired in all possible combinations. For every pair the 4-vector of the hypothesized mother particle is calculated. The number of pairs reconstructed with same sign charge in the mass region of the Z boson is representative within random fluctuations of the random combinatorics also present in the opposite sign pairs, aside from a tiny fraction of physics background described in Section 4.3.4.

The following considerations were taken into account in the selection of muon pairs:

The data analysed must be triggered by the presence of the Z -boson. This condition is met by requiring at least one muon in the muon pair to be matched to the muon trigger, with a p_T above the turnon region as seen on the right side of Figure ??.

The signal and signal to background ratio has to be optimized. This is done to a reasonable level where reduction in the number background counts remains statistically significant.

Variations in cuts are made with significant values, e.g. the p_T cut is varied with 5 GeV. This is done because varying with high granularity would likely result in a focus on a statistical fluctuation with no real physical meaning.

In Table 4.3 variations are shown in reconstruction quality (either tight or medium/loose) of the second muon and the transverse momentum cut on both muons. The mass window to define Z -candidates is between $66 < m_{\mu\mu} < 102$ GeV. In the table cases 1 and 2 show that low momenta cuts, regardless of trigger considerations, are not ideal as they result in muon samples with a high fraction of combinatorial background. The kinematic distribution of Z -decay muons however is not unfavourable to increasing the the threshold. Case 3 with two tight muons with $p_T > 5$ GeV has a good signal to background ratio which is not improved at above a statistical level by increasing the transverse momentum treshhold in case 4. The second part in the table shows whether Z -candidates can be recovered if requirement on the reconstruction quality is loosened. These qualities are called medium or loose but they are essentially defined as ‘not tight’. Case 6-9 show that a good signal to background ratio can be achieved in this reconstruction category and are indistinguishable within statistical fluctuations. The symmetric cut of case 8 is chosen to be combined with case 3, shown as case ‘3+8’ in the table, for the optimal signal to background ratio.

case	μ_1		μ_2		s	b	$\sim s/b$
	quality	p_T [GeV]	quality	p_T [GeV]			
1	trigger	5	tight	10	1180	101	12
2	trigger	10	tight	5	1128	42	27
3	trigger	10	tight	10	1080	11	98
4	trigger	10	tight	15	1057	8	132
5	trigger	10	medium or loose	20	172	38	5
6	trigger	15	medium or loose	20	148	9	16
7	trigger	20	medium or loose	15	147	4	37
8	trigger	20	medium or loose	20	142	3	47
9	trigger	20	medium or loose	25	131	3	44
3+8	trigger				1222	14	87
10	trigger	10	any	10	1282	67	19
11	trigger	20	any	20	1089	5	218

Table 4.3: Muon selection cuts with the corresponding numbers of signal and background counts.

The strength in combining two sets of kinematic cuts for different reconstruction quality categories is further illustrated in Figure 4.11. The left plot shows case 10 in yellow, 11 in blue, 3 in red and shown in black is case ‘3+8’. Both a high transverse momentum cut and a high reconstruction quality requirement are effective in reducing background. There is no need however to use both at the same time. A conditional requirement (a high momentum cut for low reconstruction quality muons) is effective at reducing background while maintaining the signal. This is also illustrated with the figure on the right which shows the cut efficiency for Z from simulation. The conditional set of cuts reaches a much higher efficiency and combines the higher efficiency of the high kinematic cut at low p_T^Z with the higher efficiency of the reconstruction quality cut at high p_T^Z .

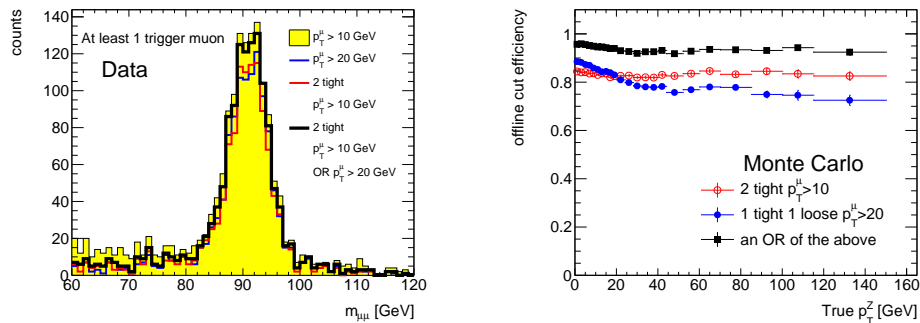


Figure 4.11: *Left*: the invariant mass of two muons after applying different muon selection cuts. *Right*: $Z \rightarrow \mu^+\mu^-$ reconstruction efficiency derived from the MC under different cut conditions.

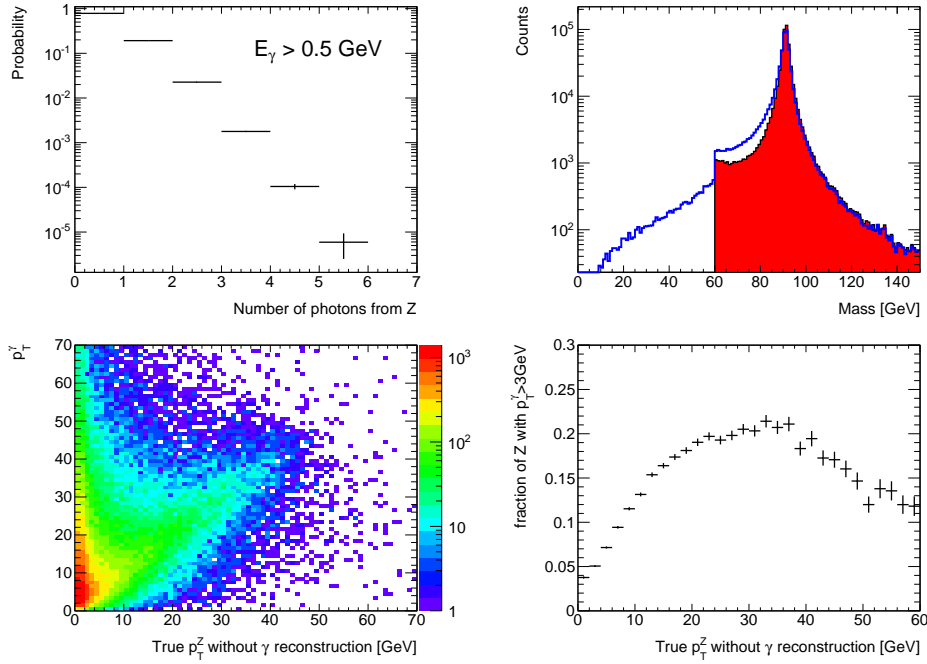


Figure 4.12: *Top left:* Probability in PYTHIA to produce n photons in the $Z \rightarrow \mu^+\mu^-$ process with the $E_T > 0.5$ GeV. The errors are statistical errors, not the error within the MC itself. *Top right:* The modified reconstructed mass spectrum (blue) due to the decay photons is compared to the generated Z masses (red). *Bottom left:* Highly energetic photons in the decay cause reconstructed Z feigning high p_T Z bosons. *Bottom right:* The fraction of Z decays involving a photon of at least $p_T^\gamma > 3$ GeV as a function of true p_T^Z without photon reconstruction.

4.3.2 $Z \rightarrow \mu^+\mu^-$ reconstruction and cut efficiencies

The PYTHIA embedded in HIJING simulation is used to study the Z efficiencies necessary to make corrections. PYTHIA simulates the Z -boson production in nucleon-nucleon collisions at $\sqrt{s_{NN}} = 2.76$ TeV in a pp:pn:np:nn configuration that reflects the proportions in lead-lead collisions. The simulation incorporates the decay to muons, which can involve the radiation of photons. Photons carry away energy from the Z boson which is not reconstructed using the 4-vectors of the decay muons. The left side of Figure 4.12 shows the probability for n photons with $p_T > 0.5$ GeV to be produced. On the right side is shown how the generated Z mass spectrum (red) is modified (blue) if radiated photons are not included with the muon daughters in the calculation of properties of the Z boson. Although efficiency loss or spectrum modifications suffered here is procedural rather than a direct result of detector properties, the corrections are applied with the simulation in the same way.

The reconstruction efficiency for the Z boson is defined in the same way as for the muons, the fraction of reconstructed Z matched to truth (through matching of the muons) divided by the number of generated Z . The cut efficiency is defined as the Z that pass the

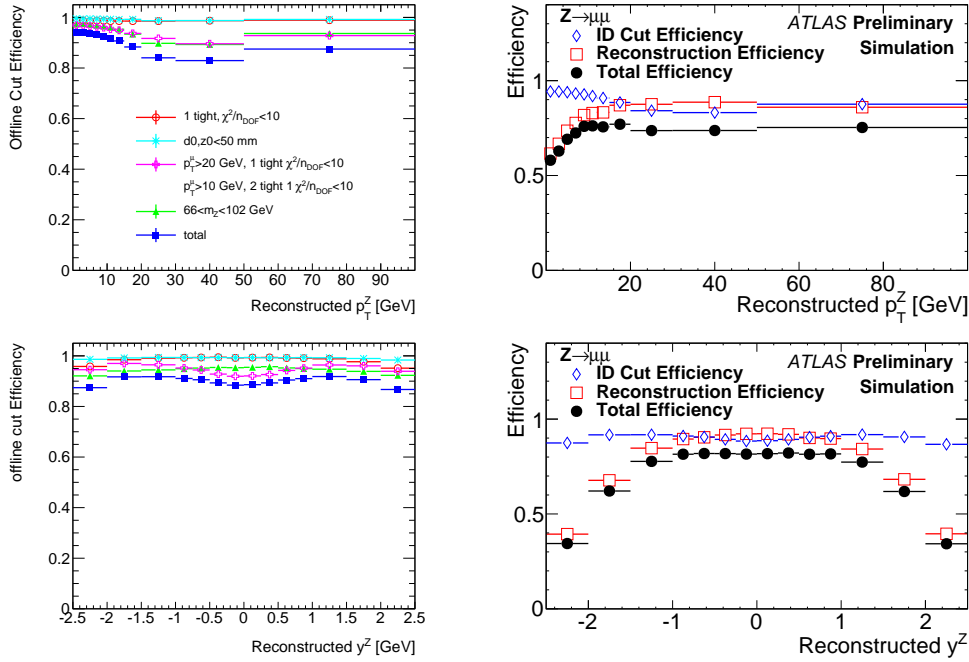


Figure 4.13: Monte Carlo efficiency curves. In the left column is shown the cut efficiency with respect to the reconstructed Z 's. In the right column is shown the reconstruction efficiency with respect to generated Z 's, the cut efficiency with respect to reconstructed Z 's and the total efficiency, which is the set of Z 's after analysis cuts with respect to all generated Z 's.

cuts divided by the Z that are reconstructed with no additional requirements. Figure 4.13 shows on the left side efficiency of the cuts used in the analysis. The requirement that one of the muons must be tight with a good ID-MS track match, representative of the trigger muon, is highly efficient, as is requiring vertex pointing within 50 mm of the primary vertex for both muons.

The conditional cut described in the previous section has a dip around 30 GeV resulting from Z kinematics. A boosted Z with $p_T^Z \sim 30$ GeV has a higher probability of a muon in the decay with low transverse momentum. The mass window cut shows a similar trend which results from spectrum modifications due to the radiated photons in the Z decay. As shown in Figure 4.12 a reconstructed Z with $p_T^Z \sim 30$ GeV has a relative large fraction ($\sim 20\%$) of energetic photons involved in the Z decay, giving a kick to the Z and hence its boost. The photon also modifies the mass spectrum of the reconstructed Z causing the lower efficiency for the mass window cut in this p_T^Z region. On the right side of Figure 4.13 the cut efficiency is shown with the reconstruction and total efficiency (cut and reconstruction combined). The low reconstruction efficiency for low p_T^Z is the result of migration of low p_T^Z towards higher transverse momentum. The efficiency curve is a combination of detector efficiency and bin migration, which is corrected for in one single step when these efficiencies are used as correction factors for the spectra. Figure 4.14 shows the efficiency as a function of event centrality. Towards

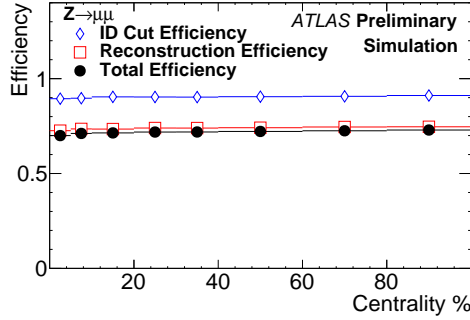


Figure 4.14: Reconstruction, cut and total efficiency for the Z boson as a function of event centrality.

higher centralities both the cut and reconstruction efficiency show a minor dip, resulting in an approximately 3% lower total efficiency for Z reconstruction in the most central events.

4.3.3 $Z \rightarrow \mu^+ \mu^-$ trigger efficiency

From the single muon trigger efficiency calculated in the Minimum Bias stream the trigger efficiency for the Z is derived. A Z is triggered if at least one of the daughter muons, with criteria described in Section 4.2.4, is matched to the muon trigger object. Z candidates with no match to the trigger ($< 1\%$) are unused in this analysis. For Z triggered by just one muon, $\epsilon_{\text{trig}}^Z = \epsilon_{\text{trig}}^\mu$. In case both muons match the trigger and satisfy the quality criteria, ϵ_{trig}^Z is evaluated according to the formula

$$\epsilon_{\text{trig}}^Z = 1 - \left(1 - \epsilon_{\text{trig}}^\mu(p_{T1})\right) \left(1 - \epsilon_{\text{trig}}^\mu(p_{T2})\right). \quad (4.3)$$

where $\epsilon_{\text{trig}}^\mu(p_T)$ is the fit result by Equation 4.1 taken at the reconstructed p_T value of each muon and at the corresponding in of centrality and rapidity from the set of 12 slices (4 in centrality and 3 in rapidity) specified in Table 4.2. The muon kinematics (transverse momentum and rapidity) in the MC were used together with this table to propagate muon efficiencies to Z trigger efficiencies including the errors. The results for the Z efficiencies in different centralities is shown in Table 4.4. ϵ_{trig}^Z as a function of rapidity and transverse momentum in shown in Figure 4.15. The dip in the p_T^Z distribution around 40 GeV, more distinctive for the most central events, is due to a small turn of the fitting curve of the contributing single muon efficiency just above 10 GeV before it comes to saturation at the plateau. Non-flat dependencies in both p_T^Z and y cause the respective trigger correction of the Z yield to be performed with corresponding two-dimensional Z trigger efficiency maps.

Centrality [%]	Trigger efficiency [%]	Centrality [%]	Trigger efficiency [%]
0-5	95.0±0.5	5-10	95.6±0.5
10-20	97.8±0.4	20-30	98.8±0.2
30-40	98.8±0.2	40-60	98.9±0.3
60-80	99.0±0.3		

Table 4.4: Z trigger efficiency ϵ_{trig}^Z in different centrality classes.

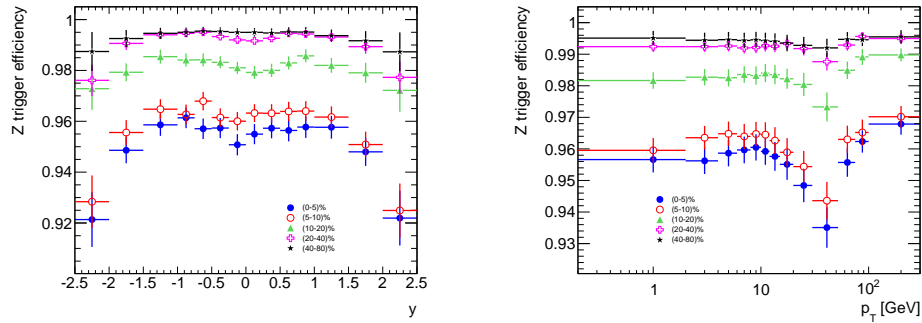


Figure 4.15: *Left*: $Z \rightarrow \mu^+\mu^-$ trigger efficiency as a function of rapidity. *Right*: the same as a function of transverse momentum.

4.3.4 Comparisons and cross-checks

Several checks have been made to verify whether the simulation correctly describes the data. This regards the kinematic distribution of the muons and the Z candidates and the reconstruction quality of the muons.

Figure 4.16 shows distribution of reconstructed muons in data and MC for (clockwise) the muon pair $\Delta\phi$, pseudo-rapidity, p_T and the muon pair opening angle. Another interesting observable is the relative properties of one muon with respect to the other muon in the pair. Figure 4.17 compares different properties of the pairs as a function of p_T , η and centrality between the data and the MC. Some of these discrepancies are used to estimate a systematic error on the cut efficiency as is described in Section 4.5.

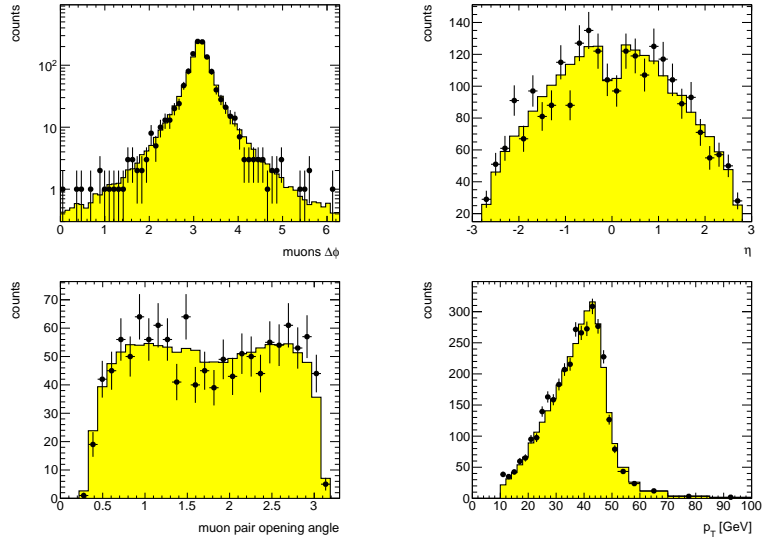


Figure 4.16: Data spectra and MC for muons. *Top left:* $\Delta\phi$ distribution of the Z daughter muons. *Top right:* η distribution. *Bottom left:* the opening angle of the muons and *bottom right:* p_T distribution.

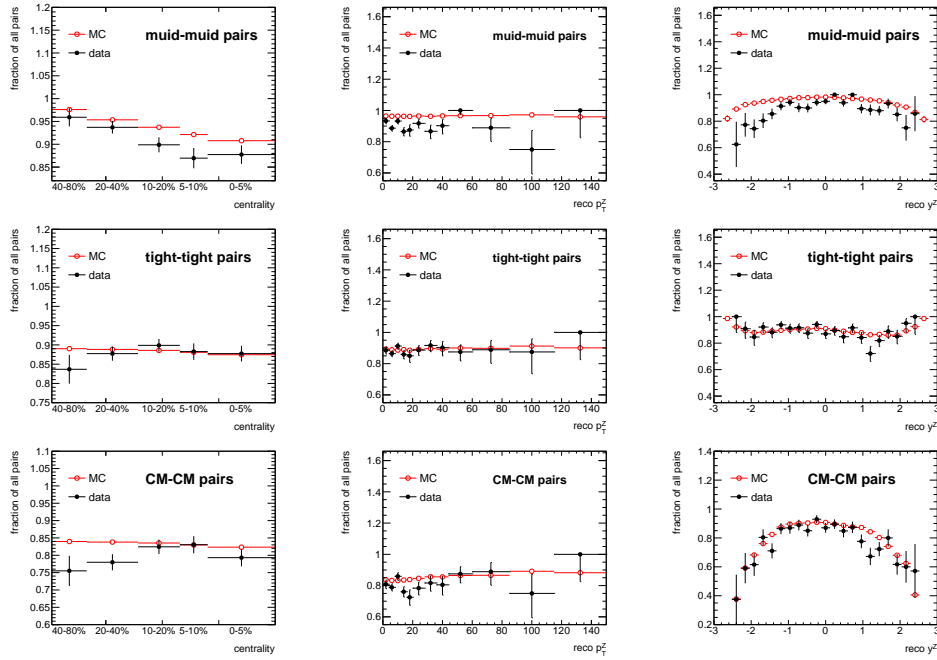


Figure 4.17: The plots show the ratio of pairs with certain properties with respect to all reconstructed pairs, as a function centrality, reconstructed Z p_T and y . Pair properties shown are muid-muid, tight-tight and combined-combined (CM-CM) muon pairs. The complementary fraction is thus mostly resp. muid-staco, tight-loose and combined-standalone pairs.

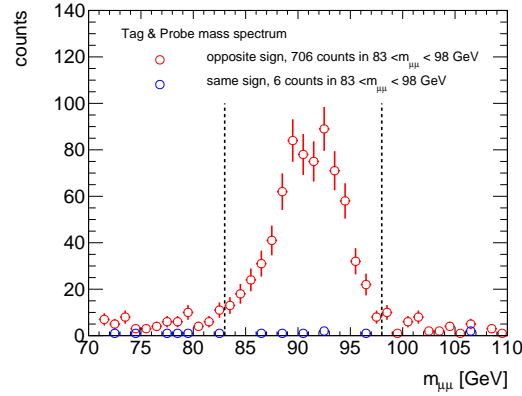


Figure 4.18: Mass spectrum for tag and probe data sample.

The Tag & Probe method is used to check the muon cut and trigger efficiency. A data sample of Z 's satisfying the requirement $83 < m_{\mu\mu} < 98$ GeV is selected by imposing very strong cuts on one muon only, the Tag. Selection criteria used for the Tag are listed below.

- CombinedMuon
- $p_T > 15$ GeV
- $n\text{PixHits} > 2$; $n\text{SCTHits} > 5$; $n\text{PixHoles} + n\text{SCTHoles} < 1$; $n\text{SCTHits} + n\text{PixHits} > 10$
- $|d_0^{ID}| < 0.2$ mm; $|z_0^{ID}| < 1.5$ mm
- $|p^{ID}/q| > 4$ GeV
- $|\eta| < 2.5$
- $\text{match } \chi^2/\text{ndof} < 3$

They provides for a Z data sample of high purity shown in Figure 4.18. In this sample, the muons associated to the Tag is with high probability a real Z daughter muon, regardless of the quality of the reconstruction. This muon, the Probe, can be used to calculate several quantities important for the analysis. Background contamination in the T&P sample mostly comes up at muons with low p_T , therefore we imposed a cut of $p_T > 15$ GeV on the second muon as well. Other shortcomings of the T&P method are very low statistics and possible Tag-Probe correlations. Therefore we use the T&P method as a cross check and worked out the real correction using the MC.

Figure 4.19 on the left shows the raw Probe p_T spectrum and the spectrum after several cuts as they are applied in the analysis. The right plot shows the total cut efficiency relative to reconstructed, which is the Probe p_T spectrum after all cuts divided by the raw spectrum. The integrated cut efficiency derived from this set is $89.4 \pm 1.2\%$.

Several distributions are shown in Figure 4.20. The MC is normalized to data by integral, except for the bottom right panel, where the absolute fractions are compared. The

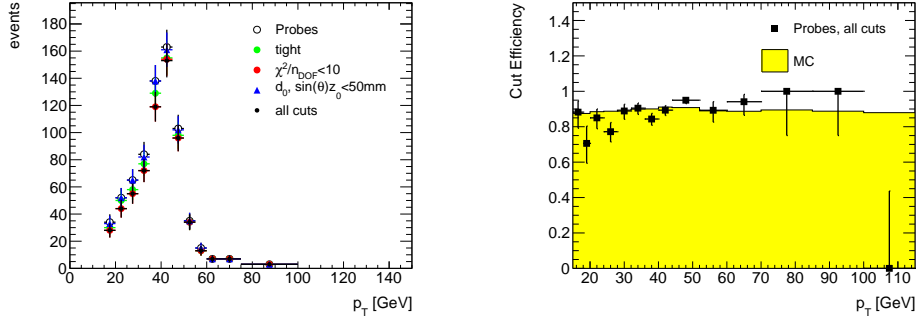


Figure 4.19: Left: Effect of cuts on the probe p_T spectrum. Right: The cut efficiency from the probes with all cuts applied from the plot on the left.

top panels show the d_0 and $z_0 \sin(\theta)$ distributions. Bottom panels show the χ^2/n_{dof} on the left and the fraction of tight muons with respect to all Z daughter muons on the right. The comparison is shown for different parts of the detector and for different centralities. The χ^2/n_{dof} plot includes a point on the right side which is for muons in data and Monte Carlo with $\chi^2/n_{dof} > 10$. This is used for standalone muons. We find a good agreement between the data and the MC within a limited sample provided by the T&P method.

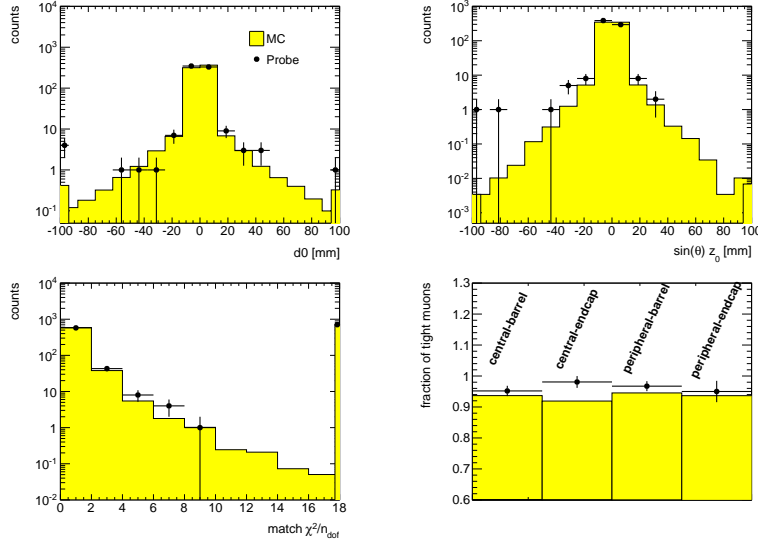


Figure 4.20: MC to T&P comparison. Top row shows d_0 and $z_0 \sin(\theta)$, bottom χ^2/n_{dof} and fraction of tight muons among all muons coming from Z in different parts of the detector and for different centralities.

Figure 4.21 shows T&P method used to evaluate single muon trigger efficiency compared to the results obtained from the MB data sample in dependence on transverse momentum and pseudorapidity, respectively. Discrepancy between the trigger efficiencies in the two methods is propagated into a systematic error. Details are in Section 4.5.

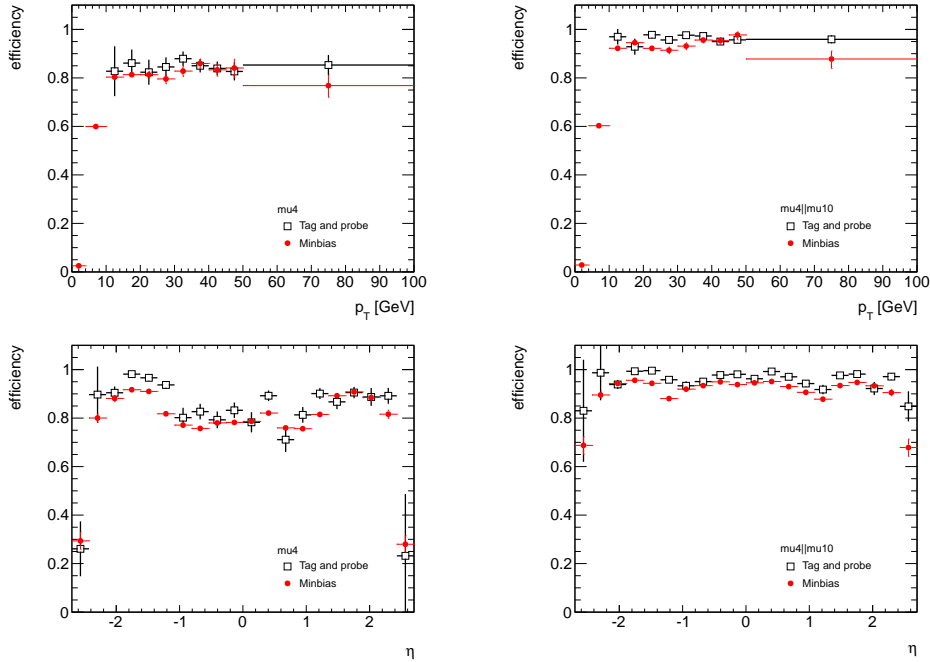


Figure 4.21: Cross check of the trigger efficiency calculated from MinBias with calculation from HardProbes stream using Tag and Probe method with Z daughter muons, for mu4 trigger (left) and mu4 OR mu10 (right), as a function of transverse momentum (top) and pseudorapidity (bottom).

4.3.5 Background contributions

Background present in the Z-candidate sample in the form of same sign pairs is taken as estimate of random combinatorial background. There are several physics processes responsible for background in the form of same sign pairs only. An estimate for the amount of same sign pairs from background processes are present in the sample is made from a fit. With `ROOT` the reconstructed MC shape is fitted to same sign subtracted data superimposed on a second ‘background’ function. Variations using linear and exponential functions with different slopes for the background deliver a consistent picture. An example is shown in Figure 4.22. The fit yields a residual background estimate of 5 ± 11 . The result is consistent to zero within its large uncertainty. Due to this fact no additional subtraction on the data are made but the uncertainty is added, together with the uncertainty related to same sign subtraction estimated conservatively at 50%, to the systematic uncertainty. This results in a total background uncertainty of $\sqrt{0.5\%^2 + 0.8\%^2} = 0.9\%$. The total background estimate of $1.1 \pm 0.9\%$ safely includes the estimated background studied by ATLAS in proton-proton data [22]:

- QCD background - 0.4%
- $t\bar{t}$ - 0.1%
- $Z \rightarrow \tau\tau$ - 0.07%

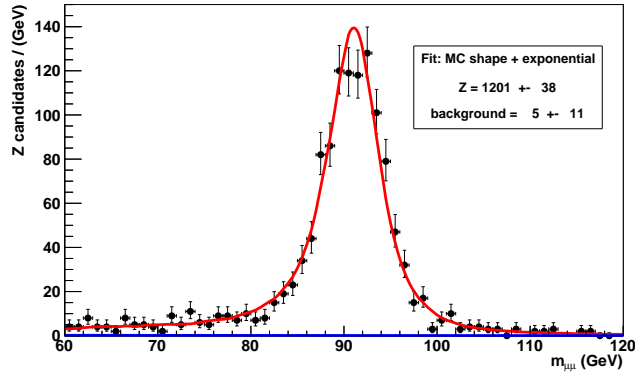


Figure 4.22: The same sign subtracted data fit with a two component model. The signal is taken from the simulation and the background (shown as an example) is exponential.

- Di-boson decays - 0.2%

One more entirely different type of background contribution can be caused by muon charge swap. The charges swapping effect was checked using the MC sample. The results are shown in Figure 4.23. The red curve is the invariant mass distribution of two muons with opposite charges matched to truth Z-bosons. Blue histogram shows truth mass for Z which are reconstructed with the same sign muons, and green shows their reconstructed mass distributions. As one can see the contribution of wrongly reconstructed same sign pairs in the Z mass region coming from real Z bosons is around 0.1%.

4.4 Correction strategy

The final result is recovered from data based on several corrections from simulation in the following way

$$Result = \frac{Signal - Background}{Correction \times Acceptance \times N_{events}}, \quad (4.4)$$

where *Signal* is the number of Z candidates found in data, *Background* the number of same sign muon pairs, *Correction* accounts for loss due to detector efficiencies and for detector resolution, *Acceptance* is the limited physical coverage of the detector for the decay particles and N_{events} is the number of events. The *Background* in the mass window is close to 1% of the of the (same sign) Z-candidates. The background was subtracted on a bin-by-bin basis and the corresponding uncertainties due to the subtraction are added to the statistical uncertainty in the bin. In the cases where quantities are studied differentially such that bin by bin fluctuations in the background may be significant the subtraction is based on the average background fraction. In this case we assign a 50% systematic uncertainty to the statistical correction. The *Acceptance* is derived from MC. The accuracy of this value depends on the ability of the generator to

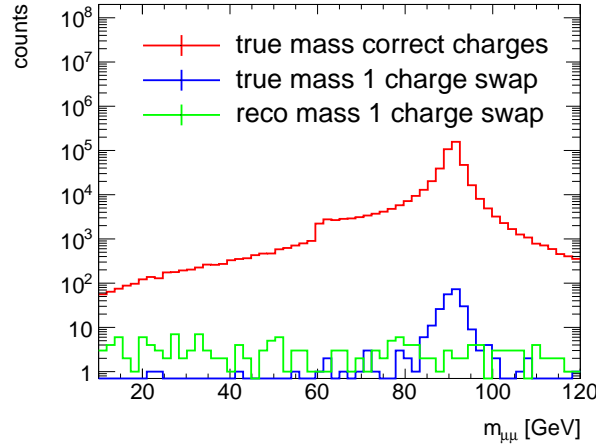


Figure 4.23: Invariant mass of $\mu^+\mu^-$ pair. Red: True mass distribution for muon pairs with correctly reconstructed charges. Blue: True mass distribution with one muon charge swapped. Green: Reconstructed mass distribution with one muon charge swapped.

simulate the rapidity of the Z bosons and the decay kinematics of the daughter muons. Both are found to be correct within negligible errors. The *Correction*, detailed in the previous sections, is applied on the basis of the rapidity and transverse momentum of the Z boson candidate and as a function of event centrality. It incorporated corrections for reconstruction efficiency, identification efficiency and kinematic smearing. Final corrections (excluding trigger efficiency) are applied from the efficiencies derived with the simulation as follows

$$\epsilon^Z(\text{cent}, p_T^{\text{reco}}, y^{\text{reco}}) = \frac{N_{\text{pass}}^Z(\text{cent}, p_T^{\text{reco}}, y^{\text{reco}})}{N_{\text{gen}}^Z(\text{cent}, p_T^{\text{true}}, y^{\text{true}})}. \quad (4.5)$$

For each bin the number of Z that pass the analysis cuts are divided, based on their reconstructed values, by the number of generated Z based on their truth values. This procedure includes the correction needed for bin migration in the spectra as a result of detector resolution. This method makes a so-called *Bin-by-Bin*-correction. Another technique for unfolding separates the correction in two stages and is in principle a better, more accurate method.

In this case first a *migration matrix* is constructed from the truth information of reconstructed particles and the generated particles, as pictured in Figure 4.24. An element M_{ij} of the matrix represents the probability that an event generated in bin j is reconstructed in bin i . The inverse of this matrix applied to the reconstructed spectra in data recovers the ‘truth’ shape. An efficiency correction based on the truth information of generated and reconstructed particles then recovers the original spectrum. This procedure requires large MC statistics to keep the uncertainties in check. These are not available in this analysis for corrections across p_T and rapidity in the various centrality slices. The Bin-by-Bin method only approximate the effect of off-diagonal entries of the migration matrix and corrects for each bin separately, thus it yields similar results

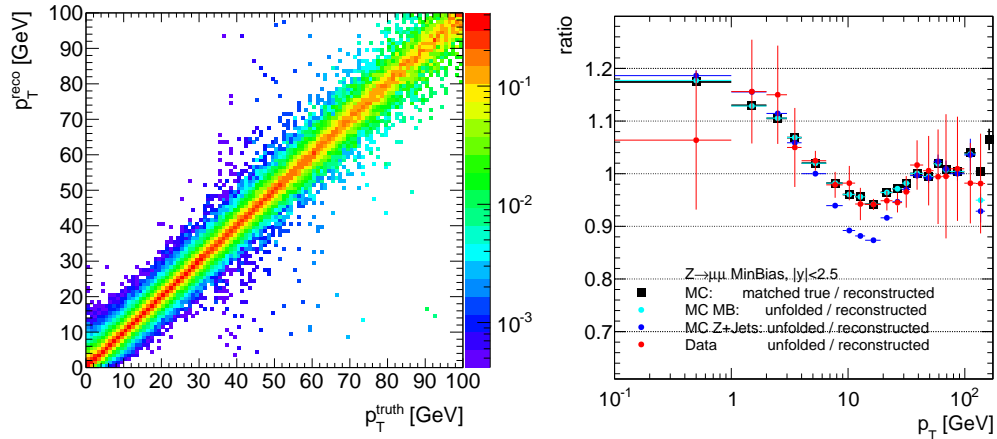


Figure 4.24: *Left*: Migration matrix. The y direction shows the probability that a Z generated with a p_T from the according x -coordinate is reconstructed in that particular bin. *Right*: Corrections for bin migration as a function of p_T^Z . Markers in black show the corrections based on the Bin-by-Bin method. Cyan markers show the effective corrections made with the migration matrix. Red markers shows that the matrix corrections applied to data are consistent with corrections applied on the MC spectrum.

if the migration matrix is not too different from the identity matrix. Shown on the right in Figure 4.24 is that this is the case. The black markers show the corrections from the Bin-by-Bin method as a function of p_T^Z . The cyan markers show corrections following unfolding with the migration matrix. Both methods yield very similar results. The unfolding applied to data, shown in red, is consistent with the black and cyan markers which reflects that the spectra shapes in MC and data are close to each other. The final *Correction* includes the trigger efficiency, which is detailed in Section [?].

4.5 Systematic uncertainties

4.5.1 Efficiency of Reconstruction and Analysis Cuts

The main uncertainty associate with efficiency correction stems from possible discrepancies between the MC and real data conditions. In a general sense these can be of two types: a) differences in the detector performance description and b) shortcomings in the physics description from PYTHIA.

In the $Z \rightarrow \mu^+\mu^-$ channel, ATLAS advises that we rely on the p+p accuracy of 1% above 15 GeV and 2% below for a single muon. This estimate is based on the low occupancy in the muon spectrometer even in the heavy ion environment. However, this accounts only for muons reconstructed purely with the muon spectrometer, muons combined with a track in the inner detector may be sensitive to tracking losses and associated uncertainty and of course some of these muons that would otherwise have inner tracks may simply be reconstructed solely in the muon arms in the heavy ion envi-

ronment. The simulation does not perfectly reproduce the composition of the different muon types reconstructed in the data (see Figure 4.17). In data the fraction of pairs with one stand alone or segment-tagged muon is higher compared to MC (respectively 20.0% and 16.8%). To address any effects that this failure of the simulation may have on the calculation of the efficiency, the simulation is adjusted by reweighting events in which two combined muons reconstruct a Z , so that the fractions in data and MC are in agreement. The efficiency is then recalculated with the weighted sample and the differences between the thus recalculated efficiency and the standard weighted one is taken as a systematic error.

In the $Z \rightarrow e^+e^-$ channel, the basic strategy for constraining the uncertainty due to discrepancies between the data and simulation is to use a data driven approach ‘Tag and Probe’ method. Section ?? describes the tag and probe method and sample, and section ?? shows the single probe electron identification efficiencies propagated into $Z \rightarrow e^+e^-$ efficiencies. There is a significant difference between the data driven $Z \rightarrow e^+e^-$ efficiency and that derived from simulation, reaching 20% at forward rapidity, which we take as a systematic uncertainty. The poor statistical precision of the probe electron method further increases the systematic uncertainty associated with the data-MC agreement, as we take the deviation at the maximal 1σ distance. Additionally we use an uncertainty of 5.5% for the uncertainty regarding the material budget.

In addition to the above mentioned uncertainty we also assign a systematic uncertainty stemming from possible disagreement with the spectral shape generated by PYTHIA (although the agreement in the spectrum at the reconstructed level is quite good - see figures ?? and ??). To estimate this uncertainty we apply the efficiency correction to the data and thus recover a corrected ‘truth’ distribution. This distribution is then used to reweight the simulation and then the reweighted simulation is used to again calculate the efficiency. Although, in principle one may iterate this procedure until convergence the fairly low statistics in the measurement makes us somewhat susceptible to fluctuations so we use only a single iteration which we then compare to the original purely PYTHIA derived efficiency for an uncertainty estimate. This uncertainty is on the order of a few percent in both the muon and electron channels.

4.5.2 Momentum Resolution

The standard Monte Carlo muon momentum resolution is unrealistically good compared to the actual detector performance. This is a known problem, generally, in ATLAS and is addressed by use of a smearing tool which accounts for imperfections of the detector alignment. The code nudges the p_T with different strengths in different regions of the detector. For an estimate of the systematic uncertainty related to the momentum resolution, additional smearing is applied to the MC. The amount of additional smearing is chosen so as to have the same width of the mass distribution in the MC as in the data. This is done by excluding events where the Z mass agreement between reconstruction and truth is better than a certain level. A parameter which reflects the

agreement is defined as:

$$\rho = \frac{|m_Z^{\text{reco}} - m_Z^{\text{truth}}|}{m_Z^{\text{truth}}}. \quad (4.6)$$

Removal of events where $\rho < 0.002$ reduces the MC statistics by 10% and brings the width of the MC and data in good agreement, see fig. 4.25. This reduced Monte Carlo

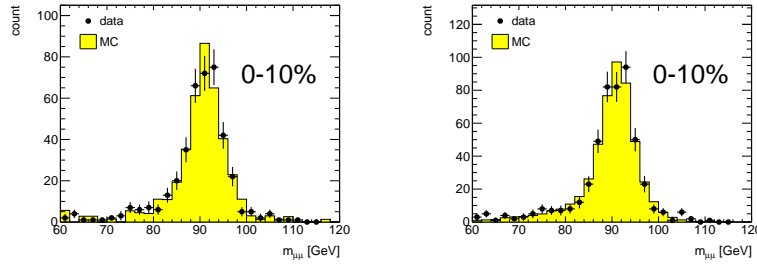


Figure 4.25: (left) Data plotted with standard MCP smeared MC. (right) Data plotted with Monte Carlo, with additional smearing ($\rho > 0.002$) applied on the Monte Carlo.

set is then used to recalculate the p_T , rapidity and centrality dependent efficiencies. The difference between the further smeared efficiency and the efficiency calculated with the standard smeared MC sample are taken as systematic errors on the order of 2-3%.

4.5.3 Trigger

The trigger chain used for the muon channel is efficient at $95.0 \pm 0.9\%$ in central and $99.0 \pm 0.6\%$. The systematic uncertainty originated from the discrepancy between the single muon efficiencies based on T&P method and the MB data sample. The comparison of the methods is shown in figures 4.21.

4.5.4 Normalization

The normalization of the overall yield depends on several pieces each with an associated uncertainty.

- Luminosity sampled - the count total number of events sampled by the minimum bias trigger has an associated uncertainty of 2% [?]
- Event count in a given centrality bin - as seen in figure 4.1 there is an uncertainty of approximately 0.3% on the centrality binned count
- Calculation of N_{coll} in a given centrality bin - N_{coll} in each bin is calculated based on a Glauber simulation and has uncertainty as shown in Table 4.1

Uncertainty Type	$Z \rightarrow \mu^+ \mu^-$ Uncertainty [%]
MC-Data Agreement	2.5
PYTHIA shape	3 - 8 (mid to forward y , higher at low p_T)
Resolution	2.5
Trigger	0.6-0.9 (peripheral to central)

Table 4.5: A summary of systematic uncertainties.

4.5.5 Other Uncertainties

Charge Misidentification

As seen in Figures 4.23 there is some charge misidentification observed in the Monte Carlo. However, it is a very small effect of approximately 0.1%.

Pileup Events

As seen in figure 4.1 the fraction of pileup events is less than 0.1%.

Wrongly Merged Muons

The merging procedure does not take detector hit information directly into account. This might lead to two reconstructed muons sharing hit information, something that is carefully managed within the MUID and STACO chains. An error here could lead to an increase of same sign muon pairs in the Z mass region. A check with STACO and MUID analysis separately showed that this effect contributes little or nothing to the same sign background in the analysis.

4.5.6 Summary of Uncertainties

Table 4.5 summarizes the systematic uncertainties. Note that there are additional bin to bin variations that are not shown here.

4.5.7 Uncertainties of the flow measurement

In the measurement of the flow the main systematic uncertainties is coming from the uncertainty of the reaction plane. This uncertainty is taken from the analysis of the reaction plane. It is shown as a gray band in fig. ???. An important cross check is to make sure that the sine term in the measurement of the flow is consistent with zero. In case it is not this term is also to be added as a systematic uncertainty of the measurement. Figure ??? demonstrates this consistency, however the statistical uncertainty is large. A non equal sine term indicates an angular shift of the particle angle w.r.t. to the EP detector and it should not depend on the particle species. Therefore this uncertainty can be taken from the hadron measurement where it is negligibly small.

In the measurement of the Z there is one more source of systematic which needs to be checked. The EP measurement can be affected by the jet correlated with the Z . To

check this phenomenon we performed the following procedure. For each event where the Z was reconstructed we studied 20 events extracted from the MB sample with the following criteria. The FCal response was required to be with 3% of the amplitude found in Z event, and the orientation of the EP was required to be within 0.3 rad of the EP orientation. The difference between Ψ^A and Ψ^C sides is shown in fig. 4.26 for three different cases.

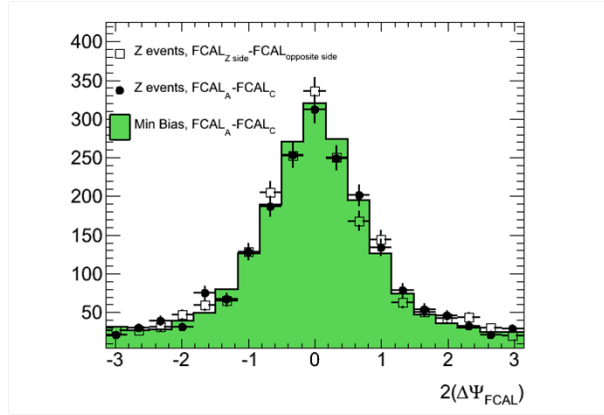


Figure 4.26: Difference in the reaction plane measured by two sides of FCal for three different cases. Green shows the MB sample selected according to the Z sample. Filled markers show the same for events with Z and open markers show that for the events with Z where the difference takes into account the direction of the Z

The green histogram shows the reference made with the MB events (without Z) according to the selection criteria explained above. The filled markers show the same distributions for the events with Z and the empty markers show the distribution for the events same event with Z but the difference is taken such that the sign of Z rapidity defines the sign of the difference. i.e. the FCal side with the same rapidity as the Z is always positive and with the opposite rapidity is negative. The mean and the widths are given in Table 4.6.

Sample	Mean	RMS
MB	0.0276 ± 0.0055	1.0909 ± 0.0039
Z without orienting	0.0032 ± 0.0254	1.1343 ± 0.0180
Z with orienting	-0.0091 ± 0.0255	1.1355 ± 0.0180

Table 4.6: Mean and RMS values for the distributions shown in fig. 4.26.

The RMS of the distribution with the Z events is 2.7σ wider than the MB distribution. This defines the EP correction which should be larger for the events with Z . We do not change the correction, but we add 4% additional uncertainty to the EP correction value. The systematic shift in the mean value between the cases with and without orienting Z is 12 mrad. Though it is less than the statistical uncertainty of the mean this difference should be added as an uncertainty to the EP angular shift due to potential impact of

jets associated with Z . Thus the systematic uncertainty on v_2 measurement is assigned 0.025.

Chapter 5

Results

The plots below show several results from the Z sample in heavy ion data.

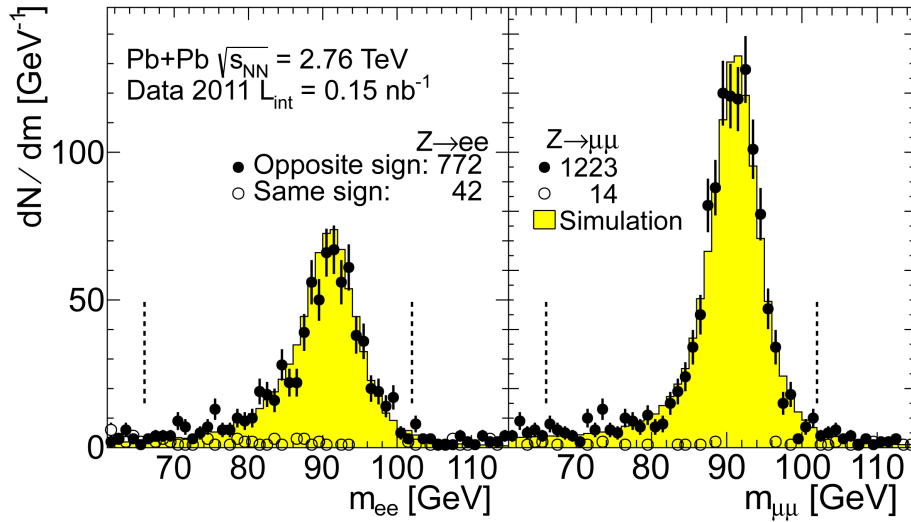


Figure 5.1: The invariant mass distribution of $Z \rightarrow ee$ and $Z \rightarrow \mu\mu$ integrated over all momentum, rapidity and centrality.

Figure 5.1 shows the mass distribution of the reconstructed Z bosons for the electron channel (left) and muon channel (right). The black disks show data and in yellow the MC. The count in the electron channel is lower due to lower detector acceptance and electron reconstruction and identification efficiency. The relatively high background results from QCD background, random combinatorics and impurity in the electron selection. The peak is broader due to lower momentum resolution and electron bremsstrahlung, an effect muons suffer less from due to their higher mass. The Z samples shown in the figure are combined for further results.

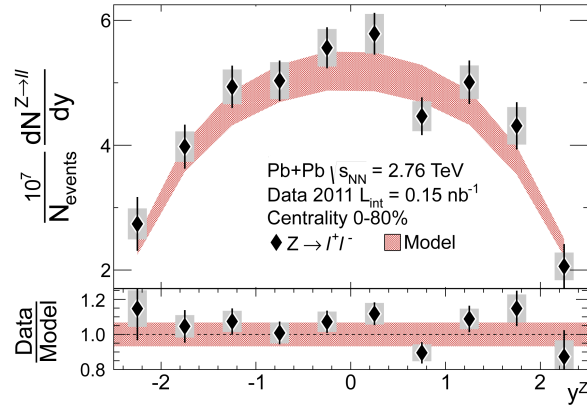


Figure 5.2: Corrected per-event rapidity distribution of measured $Z \rightarrow l^+l^-$ ($l = e, \mu$). Bars represent statistical uncertainties, the filled band represents systematic uncertainties. The data is compared to the model distribution shown as a band whose width is the normalization uncertainty.

The fully corrected rapidity distribution of the Z boson is shown in Figure 5.2, integrated over centrality and p_T^Z . The rapidity did not show any centrality dependence. The data are compared to a model composed of PYTHIA normalized to the $Z \rightarrow l^+l^-$ cross-section in p+p collisions at $\sqrt{s_{NN}} = 2.76$ TeV taken from NNLO calculations [22] and scaled by $\langle T_{AA} \rangle$. The shape is well reproduced by PYTHIA, and the integrated yield is well reproduced by the $\langle T_{AA} \rangle$ scaled NNLO cross-section.

The fully corrected p_T distributions in five centrality classes are shown in the left panel of Figure 5.3 along with the model. As was the case for the rapidity distribution, the shape in p_T^Z is well reproduced by PYTHIA. The right panel of Figure 5.3 shows the ratios of the data to the scaled PYTHIA. The ratios remain flat within uncertainties for all centrality classes over the entire range of measured p_T^Z .

Figure 5.4 shows the scaling with binary collisions of the $Z \rightarrow ee$ and $Z \rightarrow \mu\mu$ production as a function of the number of participants for $|y_Z| < 2$ and in p_T classes $p_T^Z < 10$ GeV, $10 < p_T^Z < 30$ GeV, $p_T^Z > 30$ GeV and integrated over p_T^Z . Despite a small dip in the most central bin it does not appear significant considering the statistical and systematic error. Overall both the muon and electron channel show a good agreement with binary scaling.

Figure 5.5 shows the fully corrected v_2 as a function of rapidity, centrality and p_T . The integrated v_2 of the Z boson is measured to be $v_2 = -0.011 \pm 0.018(\text{stat.}) \pm 0.014(\text{sys.})$, and is consistent with zero over the full ranges of rapidity, p_T^Z , and N_{part} . This observation is an independent measurement consistent with binary collision scaling.

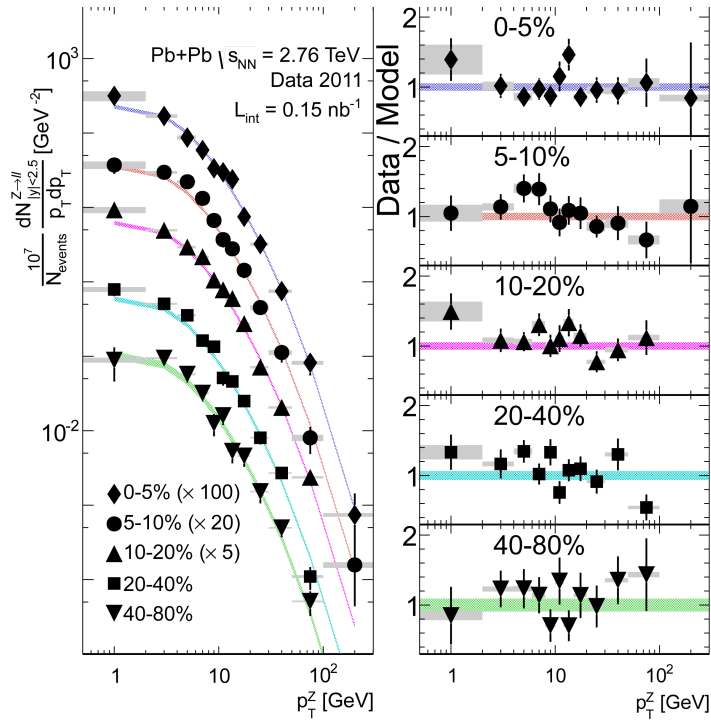


Figure 5.3: *Left*: Fully corrected per-event p_T^Z distributions in five centrality classes. Bars represent statistical uncertainties, filled bands represent systematic uncertainties. The data are compared to a model of PYTHIA normalized to the NNLO cross-section and scaled by $\langle T_{AA} \rangle$, shown in bands whose width is the normalization uncertainty. *Right*: Ratios of the data to the model.

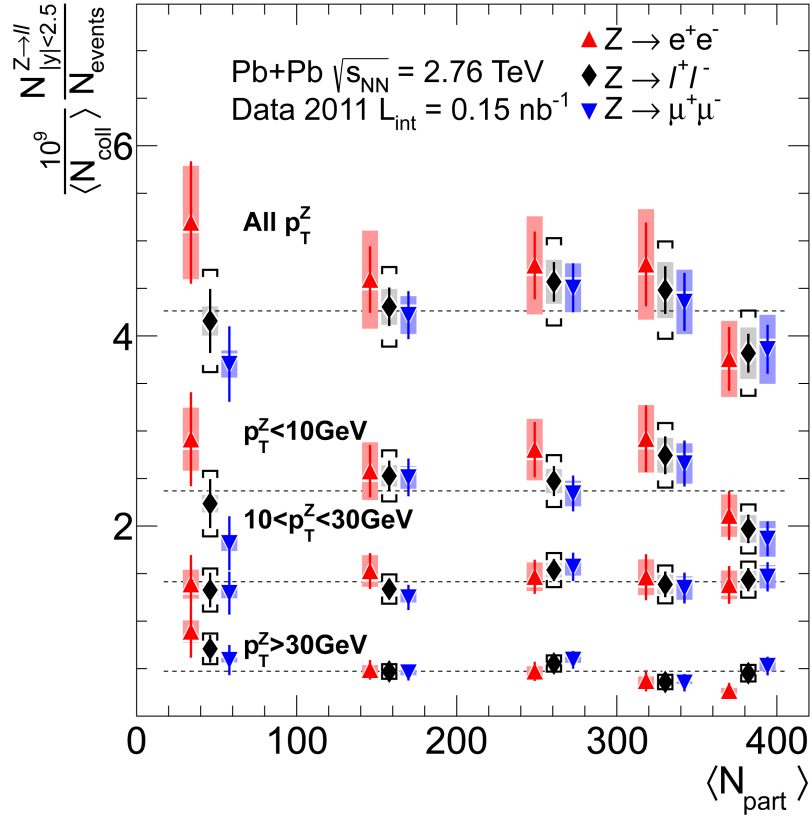


Figure 5.4: Centrality dependence of Z boson yields divided by N_{coll} . Results for ee (upward pointing triangles) and $\mu\mu$ (downward pointing triangles) channels are shifted left and right, respectively, from their weighted average (diamonds). Bars and shaded bands represent statistical and systematic uncertainties, respectively. Brackets show the combined uncertainty including the uncertainty on N_{coll} . Fits to the combined results by a constant are shown with dashed lines.

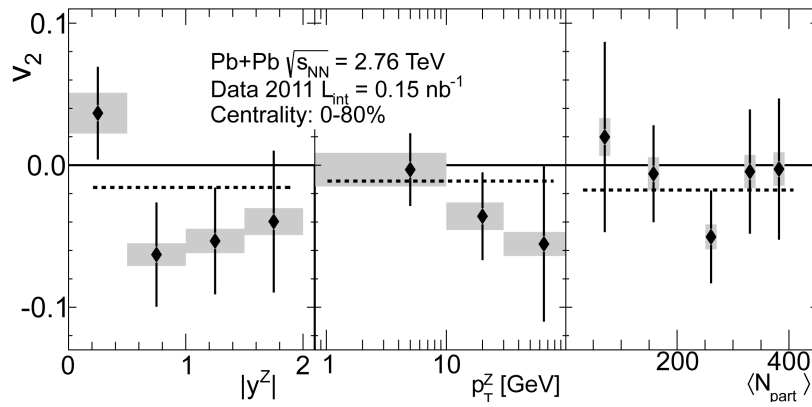


Figure 5.5: The v_2 as a function of $|y_Z|$ (left), p_T^Z (center), and N_{part} (right). Bars and shaded bands represent statistical and systematic uncertainties, respectively. The dashed lines show constant fits to the v_2 values, weighting the measurements by statistical uncertainties only.

5.1 Summary and Conclusion

With the ATLAS detector lead-lead collisions at $\sqrt{s_{NN}} = 2.76$ TeV were measured. A sample of 1223 Z bosons with purity at a level of 1% was reconstructed through the muon decay channel. The sample was used to measure transverse momentum (p_T) and rapidity (y) spectra of the Z bosons. The per-event production rate was measured as a function of event centrality. Additionally the elliptic anisotropy v_2 of the Z boson was measured. Corrections to account for detector acceptance and efficiencies we calculated from a PYTHIA $Z \rightarrow \mu^+\mu^-$ sample embedded in HIJING events. The efficiency of the ATLAS detector for the measurement of a $Z \rightarrow \mu^+\mu^-$ decay is approximately 75%. The corrections were cross checked with the Tag and Probe method and with the muon pair quality composition. The data analysed was collected in a trigger stream searching for high transverse momentum muons. The efficiency of the trigger, ranging from 95 to 99%, was calculated from a minimum bias data set.

The shape of the corrected p_T and rapidity spectra is well reconstructed by PYTHIA. The binary collision scaling of the data, where the Z boson per-event yield was divided by N_{coll} , demonstrates that the yield is consistent with the binary collision estimation from the Glauber model. The flow value v_2 , whose main uncertainties are statistical and resulting from event plane resolution, is consistent with zero over the full measured p_T and y range. These results form a firm foundation for further measurements related to the Z boson, such as Z -jet events.

Acknowledgements

The research for this master thesis was conducted at the Weizmann Institute of Science in Rehovot, Israel. I want to thank Itzhak Tserruya and Sasha Milov for welcoming me in the heavy ion group at the institute and for the opportunity to take part in frontier research in particle physics. Sasha as chair of the Z analysis has been relentless in his motivation for this study and was always available for discussions and explanations, including late-night lectures on accelerator physics. The guidance of Zvi Citron was essential for the muon analysis and its conclusion. Working with Zvi has been a great pleasure throughout the year, with his great understanding and useful advice. Besides work life I want to thank all members of the group for inviting me into their homes, most notably Itzhak for the delicious and exciting traditional Pesach Seder with his family. Arkadi Taranenko has been a great help in thinking about post-thesis plans, which resulted in a position at GSI. Finally I want to thank my family and Stefanie for supporting me throughout my stay abroad. Stefanies visits, which included a roadtrip through this beautiful and fascinating region, were the highlights of the year.

Bibliography

- [1] M. J. Tannenbaum Rep. Prog. Phys. **69** (2006) 2005–2059.
- [2] B. Müller, J. Schukraft, and B. Wyslouch Annual Review of Nuclear and Particle Science **62** (2012) .
- [3] PHENIX Collaboration, S. Adler et al., *Centrality Dependence of Direct Photon Production in $\sqrt{s_{NN}} = 200$ GeV Au + Au Collisions*, Phys. Rev. Lett. **94** (Jun, 2005) 232301.
<http://link.aps.org/doi/10.1103/PhysRevLett.94.232301>.
- [4] ATLAS Collaboration, *Measurement of the centrality dependence of J/ψ yields and observation of Z production in lead-lead collisions with the ATLAS detector at the LHC*, Phys. Lett. **B697** (2011) 294–312, arXiv:1012.5419 [hep-ex].
- [5] CMS Collaboration, *Weak boson production measured in PbPb and pp collisions by CMS*, J. Phys. **G38** (2011) 124132, arXiv:1109.0594 [nucl-ex].
- [6] ATLAS Collaboration, *Measurements of W Boson Yields in Pb+Pb at 2.76 TeV/nucleon via single muons with the ATLAS detector*, ATLAS-CONF-2011-078 (2011) . <http://cdsweb.cern.ch/record/1353227>.
- [7] ATLAS Collaboration, *Measurement of high p_T isolated direct photons in lead-lead collisions at $\sqrt{s_{NN}}=2.76$ TeV with the ATLAS detector at the LHC*, ATLAS-CONF-2012-051 (2012) .
- [8] ATLAS Collaboration, *Correlations between Z bosons and jets in 2.76 TeV/nucleon heavy ion collisions in ATLAS at the LHC*, ATLAS-CONF-2012-119 (2012) . <https://atlas.web.cern.ch/Atlas/GROUPS/PHYSICS/CONFNOTES/ATLAS-CONF-2012-119/>.
- [9] M. Aharrouche, A. Arbusov, et al., *Double differential Z,W cross sections and their ratios in the electron channels*, .
- [10] ATLAS Collaboration, *Measurement of the inclusive W^\pm and Z/γ^* cross sections in the e and μ decay channels in pp collisions at $\sqrt{s}= 7$ TeV with the ATLAS detector*, Phys. Rev. **D85** (2012) 072004, arXiv:1109.5141 [hep-ex].
- [11] J. Beringer et al. (Particle Data Group) Phys. Rev. **D86** (2012) .
<http://pdg.lbl.gov>.

- [12] M. Karnevskiy, *Measurement of the Z boson production with the ATLAS experiment at the LHC*, DESY-THESIS-2012-016 .
- [13] A. Biallas, M. Bleszynski, and W. Czyż, *Multiplicity distributions in nucleus-nucleus collisions at high energies*, Nuclear Physics B **111** (1976) no. 3, 461 – 476. <http://www.sciencedirect.com/science/article/pii/0550321376903291>.
- [14] D. Kharzeev, C. Lourenco, M. Nardi, and H. Satz, *A Quantitative analysis of charmonium suppression in nuclear collisions*, Z.Phys. **C74** (1997) 307–318, [arXiv:hep-ph/9612217](https://arxiv.org/abs/hep-ph/9612217) [hep-ph].
- [15] B. Alver, M. Baker, C. Loizides, and P. Steinberg, *The PHOBOS Glauber Monte Carlo*, [arXiv:0805.4411](https://arxiv.org/abs/0805.4411) [nucl-ex].
- [16] *Observation of a Centrality-Dependent Dijet Asymmetry in Lead-Lead Collisions at $\sqrt{s_{NN}} = 2.76$ TeV with the ATLAS Detector at the LHC.*, Phys. Rev. Lett. **105** (Nov, 2010) 252303. 19 p.
- [17] ATLAS Collaboration, *Measurement of the centrality dependence of charged particle spectra and RCP in lead-lead collisions at $\sqrt{s_{NN}} = 2.76$ TeV with the ATLAS detector at the LHC*, .
- [18] PHENIX Collaboration, K. Adcox et al., *Formation of dense partonic matter in relativistic nucleus-nucleus collisions at RHIC: Experimental evaluation by the PHENIX collaboration*, Nucl. Phys. **A757** (2005) 184–283, [arXiv:nuc1-ex/0410003](https://arxiv.org/abs/nuc1-ex/0410003) [nucl-ex].
- [19] ATLAS Collaboration, *Measurement of the azimuthal anisotropy for charged particle production in $\sqrt{s_{NN}} = 2.76$ TeV lead-lead collisions with the ATLAS detector*, [arXiv:1203.3087](https://arxiv.org/abs/1203.3087) [hep-ex].
- [20] ALICE Collaboration, *Suppression of charged particle production at large transverse momentum in central Pb+Pb collisions at $\sqrt{s_{NN}}$* , Physics Letters B **696** (2011) no. 1–2, 30 – 39. <http://www.sciencedirect.com/science/article/pii/S0370269310013973>.
- [21] R. Nicolaidou, L. Chevalier, S. Hassani, J. F. Laporte, E. L. Menedeu, and A. Ouraou, *Muon identification procedure for the ATLAS detector at the LHC using Muonboy reconstruction package and tests of its performance using cosmic rays and single beam data*, Journal of Physics: Conference Series **219** (2010) no. 3, 032052. <http://stacks.iop.org/1742-6596/219/i=3/a=032052>.
- [22] ATLAS Collaboration, *Measurement of the inclusive W^\pm and Z/γ^* cross sections in the e and μ decay channels in pp collisions at $\sqrt{s} = 7$ TeV with the ATLAS detector*, Phys. Rev. D **85** (2012) 072004. <http://link.aps.org/doi/10.1103/PhysRevD.85.072004>.